Characterising Drainage Multiphase Flow in Heterogeneous Sandstones

S.J. Jackson*, S. Agada, C. A. Reynolds, S. Krevor

Department of Earth Science & Engineering, Imperial College London, London, United Kingdom.

Abstract

In this work, we analyse the characterisation of drainage multiphase flow properties on heterogeneous rock cores using a rich experimental dataset and mm-m scale numerical simulations. Along with routine multiphase flow properties, 3D sub-metre scale capillary pressure heterogeneity is characterised by combining experimental observations and numerical calibration, resulting in a 3D numerical model of the rock core. The uniqueness and predictive capability of the numerical models are demonstrated by accurately predicting the experimentally measured relative permeability of N_2-DI water and CO_2-brine systems in two distinct sandstone rock cores across multiple fractional flow regimes and total flow rates. The numerical models are used to derive equivalent relative permeabilities, which are upscaled functions incorporating the effects of sub-metre scale capillary pressure. The functions are obtained across capillary numbers which span four orders of magnitude, representative of the range of flow regimes that occur in subsurface CO_2 injection. Removal of experimental boundary artefacts allows the derivation of equivalent functions which are characteristic of the continuous subsurface. We also demonstrate how heterogeneities can be re-orientated and restructured efficiently to obtain large amounts of information about expected flow regimes through different small-scale rock structures. This analysis shows how combined experimental and numerical characterisation of rock samples can be used to derive equivalent flow properties from heterogeneous rocks.

1. Introduction

Fluid flow in the subsurface is dominated by rock heterogeneity where the length scale of heterogeneity ranges from nanometres to kilometres (Ringrose and Bentley, 2015). Rock heterogeneities at the sub-metre scale, such as laminae (mm) and bedding (cm), have a large impact on single and multiphase fluid flow properties, and are considered to be one of the largest controls on flow at larger scales (Corbett et al., 1992; Ringrose and Corbett, 1994; Nordahl et al., 2005; Li and Benson, 2015). Incorporating accurate heterogeneous flow properties into reservoir characterisation is therefore crucial to the successful modelling and prediction of fluid flow in the subsurface (Saad et al., 1995), which is important for applications such as groundwater hydrology, petroleum engineering and carbon sequestration (Ringrose and Bentley, 2015).

A key component in the characterisation effort is the sampling of rock cores directly from the subsurface and derivation of flow properties at the mm-m scale in the laboratory (McPhee et al., 2015). For single phase flow, core analysis involves the evaluation of porosity and absolute permeability (McPhee et al., 2015). When multiple fluid phases are involved, capillary pressure and relative permeability relationships are also characterised (Dumore and Schols, 1974; Honarpour et al., 1986; Bachu and Bennion, 2008; Krevor et al., 2012; Pini and Benson, 2013b). Since the multiphase flow properties depend on the fractional pore occupancy of the fluid phases, i.e. the saturation, the hysteretic nature of the functions (due to cyclic conditions) and the trapping of fluid phases are also evaluated (Oak, 1980; Fulcher Jr. et al., 1985; Pentland et al., 2011; Akbarabadi and Piri, 2012; Pini and Benson, 2017).

The theoretical justification for the use of flow properties derived from rock core analysis is based in Effective Medium Theory; see Renard and de Marsily (1997) and more recently Ringrose and Bentley (2015) for reviews. Measurements of flow properties must be made in a representative elementary volume (REV) of material, whereby

*Corresponding author

Email address: samuel.jackson@imperial.ac.uk (S.J. Jackson)

the length scale over which the macroscopic properties are derived is larger than the length scale of any heterogeneity within the REV. We draw the distinction here between *effective* properties, which are generally upscaled quantities where the heterogeneity is much smaller than the averaging scale and *equivalent* properties, where this separation of scales cannot be strictly defined (Durlofsky, 1991; Dagan et al., 2013). Equivalent properties are both flow rate and heterogeneity dependent, with the large scale flow affected in the same manner as it would be in the reservoir (Renard and de Marsily, 1997).

For multiphase flow properties, the REV for the system is not always clear (Armstrong et al., 2014), especially in the presence of laminae (mm) or bedding (cm) scale heterogeneities (Corbett et al., 1992). In the presence of large heterogeneities, i.e. approaching the scale of observation, effective multiphase flow properties cannot be obtained (Renard and de Marsily, 1997). As a result, most laboratory observations of multiphase flow properties are required to be obtained from homogeneous and isotropic rock samples. Measurements of relative permeability are generally performed at high flow rates so that homogeneous saturations are obtained throughout the core. This provides a measurement of the rate-invariant relative permeability in the viscous limit.

The viscous limit relative permeability is often referred to as 'intrinsic' (Reynolds and Krevor, 2015), 'characteristic' (Krause and Benson, 2015), or as a 'rock curve' (Pickup and Stephen, 2000), due to its association with universality. However, as we will demonstrate in this work, the characterisation of a rock core solely with this viscous limit relative permeability has little relevance for the description of subsurface flow in heterogeneous rocks, and should be replaced with equivalent relative permeabilities derived on representative rocks at appropriate reservoir conditions.

Deriving equivalent functions experimentally, although theoretically possible, places severe demands on the experimental observation. The experiment must be performed with flow rates, fluid pairs, fluid properties and the orientation of rock heterogeneity with respect to flow as they are in the reservoir (Reynolds and Krevor, 2015). It is not feasible to derive these functions across a large range of conditions; as a result no attempts have been made to develop a protocol for effectively measuring properties on heterogeneous rocks. In this work we show that advances in both core flood experiments and numerical simulation can be combined to overcome the problems associated with deriving equivalent properties on heterogeneous rocks.

A number of studies have shown how saturation heterogeneity, and thus relative permeability heterogeneity, will arise in rocks with small variations in capillary pressure characteristics (Ringrose et al., 1993; Honarpour et al., 1995; Huang et al., 1995; Egermann and Lenormand, 2005; Krause and Benson, 2015). These heterogeneities are often small enough (i.e. $\Delta P_c < 1$ kPa) for the core to be considered homogeneous when evaluated with single phase tracer tests (Reynolds and Krevor, 2015). Although initially focused on oil production, the study of capillary pressure heterogeneity has more recently shifted to understanding gas-water systems associated with CO_2 storage. In these systems, the impact of capillary pressure heterogeneity has been demonstrated experimentally at both the core scale, i.e. Perrin and Benson (2010); Krevor et al. (2011); Shi et al. (2011); Wei et al. (2014) and at intermediate scales below seismic resolution (1-10m) using meter-scale experiments (Trevisan et al., 2017b). Here, it was explicitly shown how layered capillary heterogeneities could increase non-wetting phase trapping by up to 15% in some cases and lead to plume migration time scales of the order of months as opposed to weeks in the homogeneous case.

Numerical simulations at the cm-m scale in gas-water systems have demonstrated the impact of local capillary pressure heterogeneity, which can immobilise a buoyant CO_2 plume under limited CO_2 supply (Li and Benson, 2015), channel CO_2 through a small fraction of the domain (Meckel et al., 2015) and significantly increase the overall trapping of CO_2 compared to residual trapping alone (Saadatpoor et al., 2010). Furthermore, at the reservoir scale, only capillary flow models can effectively describe the Sleipner field CO_2 plume evolution in the northern North Sea (Cavanagh and Nazarian, 2014), and early breakthrough at the Frio injection site is thought to be largely due to preferential capillary pressure pathways (Hovorka et al., 2006). It is therefore clear that capillary pressure heterogeneities, occurring at length scales of mm-cm, significantly impact the flow and trapping of CO_2 from the laboratory to the field scale, and need to be accurately characterised and incorporated into subsurface modelling efforts.

Incorporating small scale capillary heterogeneity into simulations at the reservoir scale requires upscaling to be performed, due to the limitations of grid size in numerical modelling. In upscaling procedures, the fine-scale flow functions are averaged at a larger scale, either analytically or numerically, to reduce computation cost whilst maintaining the underlying physical attributes of the fine-scale flow (Rabinovich et al., 2015). While most upscaling efforts focus on upscaling heterogeneous permeability distributions (Holden and Nielsen, 2000; Jackson et al., 2003) or relative permeability (Barker and Dupouy, 1999; Gasda and Celia, 2005), only recently have strong capillary pressure heterogeneity effects been incorporated (Rabinovich et al., 2015). When capillary pressure heterogeneity is incor-

porated into a dynamic upscaling procedure (as opposed to using simpler capillary or viscous limit upscaling), the resulting equivalent relative permeability is both flow rate and heterogeneity dependent, i.e. dependent on the capillary number (Virnovsky et al., 2004; Rabinovich et al., 2015; Odsæter et al., 2015). Making use of such a modelling framework, however, requires the development of laboratory based characterisation protocols from which the properties of capillary heterogeneity, and their impacts on multiphase flow are initially derived.

Recent work has demonstrated that fluid saturation heterogeneity observed in rock cores using medical X-ray imaging can be used as a sensitive measure to characterise capillary pressure heterogeneity at the REV scale (Egermann and Lenormand, 2005; Pini et al., 2012; Pini and Benson, 2013a; Krause et al., 2013; Reynolds and Krevor, 2015). We build on these experimental approaches and combine this with recently developed modelling techniques, primarily those of Krause (2012); Krause et al. (2013); Krause and Benson (2015), to create a numerical representation of the rock core. The numerical models are then used to derive equivalent relative permeabilities at a range of conditions that are relevant to the subsurface.

Under this paradigm, the goal of the characterisation shifts. Conventionally, the focus of core analysis is on obtaining the most accurate viscous limit relative permeability curve directly from experimental core floods (i.e. at very high flow rates in homogeneous cores). Recent modelling efforts have similarly focused on deriving the viscous limit relative permeability from observations on heterogeneous rocks (Krause and Benson, 2015). In the approach presented here, the goal becomes to characterise a numerical rock core with accurate viscous limit properties, and use this to derive equivalent relative permeabilities at relevant reservoir and flow conditions, which are suitable for upscaling and field scale reservoir simulation.

In the following, we characterise the drainage multiphase flow properties of a Bentheimer and Bunter sandstone core with differing principal orientations of capillary heterogeneity. Routine properties such as porosity, absolute permeability and viscous limit relative permeability are first derived from high flow rate core flood experiments and 1D numerical simulations in sections 2.1 and 2.2. 3D Capillary pressure heterogeneity is then derived through the calibration of a numerical representation of the rock core against X-ray imagery of fluid saturation data obtained during steady state core flooding experiments. The numerical models are used to predict the equivalent relative permeabilities across a range of capillary numbers, and compared directly to experimental measurements in sections 3.1 to 3.3. Finally, in section 3.4, we use the numerical models to predict equivalent relative permeabilities without the constraints imposed by the experimental observations: we remove boundary artefacts, control the structure/orientation of the heterogeneity and perform numerical experiments under conditions impractical to produce in the laboratory.

2. Characterisation of multiphase flow properties on heterogeneous cores

Two sandstone cores are used to demonstrate the characterisation approach on heterogeneous rocks, with properties detailed in Table 1. We use a Bentheimer sandstone with a simple heterogeneity parallel to the axis of flow as described in (Reynolds and Krevor, 2015), and a Bunter sandstone with primary heterogeneities perpendicular to the flow as described in (Reynolds et al., 2017). The Bentheimer sandstone is a shallow marine sandstone which forms the unit for oil reservoirs in the Netherlands and Germany. It is frequently used in petrophysical studies due to its availability in quarries, high permeability, and homogeneity (Peksa et al., 2015). The sample was composed of 95% fine to medium grained quartz with a well-sorted grain size distribution and minor feldspar and clays (5%).

The Bunter sandstone sample is a medium-grained sandstone composed mainly of sub-angular to sub-rounded quartz grains with a minor component of detrital K-feldspar, clay, and carbonate clasts with a well sorted grain size distribution. The core sample was obtained from the British Geological Survey Core Store, drilled from the Cleethorpes-1 geothermal borehole at 1312 m depth.

Since this work is motivated by the impact of sub-metre scale rock heterogeneity on multiphase flow characterisation, we focus on gas-liquid systems at elevated pressures and temperatures, equivalent to those in typical subsurface reservoirs suitable for carbon sequestration (Krevor et al., 2012). In these systems, low flow potential gas plumes are significantly impacted by capillary pressure heterogeneity (Saadatpoor et al., 2010), which can result in equivalent relative permeabilities which are far from the viscous limit values (Li and Benson, 2015; Rabinovich et al., 2015). We use both Nitrogen - DI water and CO_2 - Brine fluid pairs, so that the impact of capillary pressure heterogeneity can be clearly demonstrated independently of variations caused by the choice of fluid pair. The nitrogen system is chemically inert, and more accurate to image due to the large density contrast between nitrogen and water. The use of nitrogen

Parameters	Bentheimer	Bunter
Non-wetting phase, *nw*	N_2	CO_2
Wetting phase, *w*	DI water	Brine
Q_{tot} high/low [ml.min^{-1}]	40/7	20/0.2
# fractions high/low [-]	10/6	8/5
Pressure, P [MPa]	15.5	13.1
Temperature, T [°C]	50	53
nw density, ρ_{nw} [kg.m^{-3}]	155.0	604.4
w density, ρ_w [kg.m^{-3}]	996.5	1021.9
nw viscosity, μ_{nw} [μ Pa.s]	22.1	45.9
w viscosity, μ_w [μPa.s]	549.9	581.6
IFT, γ [mN/m]	62	34.7
Core length, L [m]	0.198	0.151
Core radius, r [m]	0.01905	0.01905
Voxel Δx & Δy [m]	0.001875	0.001875
Voxel Δz [m]	0.005	0.003
Core slices/# voxels [-]	39/6708	49/8428
Entry pressure, P_e [kPa]	3.51	1.62
Pore distribution, λ [-]	2.3	1.43
Porosity, ϕ [-]	0.207	0.249
Permeability, K_{abs} [D]	1.86	2.20
Chierici k_r A/B [-]	3/5	3/3.75
L/M [-]	0.75/0.65	0.9/0.4
$k_{rg}(S_{wirr})/k_{rw}(S_{gc})$ [-]	1/1	1/1
S_{wirr}/S_{gc} [-]	0.081/0.0	0.082/0.0

Table 1: Experimental and numerical modelling parameters used in the characterisation approach.

also precludes vigorous cleaning of rock cores between observations which boosts precision in repeat experiments on the same rock core. The CO_2 - brine systems, although experimentally more challenging, allow the exploration of real carbon sequestration fluids at the temperatures and pressures associated with the subsurface.

The importance of capillary heterogeneity in controlling fluid flow depends on the ratio of the viscous or bouyant flow potential to gradients in capillary pressure induced by rock heterogeneity, which can be described with a macroscopic capillary number. In this work, we use the macroscopic capillary number N_c presented in Virnovsky et al. (2004) to guide our characterisation efforts:

$$N_c = \frac{H}{L}\frac{\Delta P}{\Delta P_c} \tag{1}$$

where ΔP is the pressure drop over a macroscopic length scale L and ΔP_c is the characteristic difference in capillary pressure between regions separated by heterogeneity length H. For the systems considered in this work, ΔP_c can be estimated using the difference in entry pressure between the high and low entry pressure regions, with corresponding heterogeneity length scale H. With this and the measured pressure drops, the capillary number can be estimated for the core floods.

This capillary number indicates the transition from a capillary dominated regime (low N_c), where the fluid saturation is controlled by capillary pressure heterogeneity, to a viscous dominated regime (high N_c) where the fluid saturation is primarily controlled by the distribution of absolute and relative permeabilities. The more widely used capillary number $n_c = v\mu/\gamma$ is indicative of the average balance of viscous and capillary forces at the scale of individual pores. In the absence of chemical surfactants, even corefloods at flow rates much higher than those found in the subsurface exhibit $n_c < 10^{-6}$, and capillarity is dominant at the scale of individual pores. It is the core scale capillary number N_c that provides useful information about the impact of rock heterogeneity.

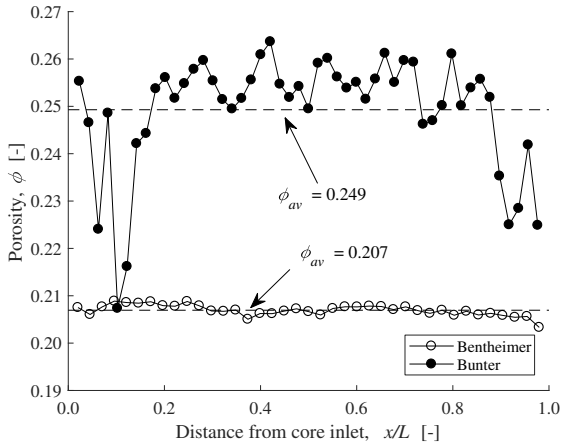

Figure 1: Slice average porosity of the rock samples used in this study along the length of the rock cores.

To characterise the viscous limit relative and absolute permeability, we require N_c to be large, in a regime nearing the viscous limit. This ensures that the core has a near homogeneous, 1D saturation profile through the length of the core, and the relative permeability can be accurately derived without prior knowledge of the 3D capillary pressure heterogeneity. In the high flow rate regimes considered here for the Bunter and Bentheimer, the maximum N_c across the fractional flow regime is of the order $10^1 - 10^2$ respectively (see section 3.4), which is similar to the viscous limit transition region identified by Reynolds and Krevor (2015) and Reynolds et al. (2017) of $10 < N_c < 75$. In this viscous dominated regime, the slice average saturations are largely homogeneous; see Figure 25 in Reynolds and Krevor (2015) and Figure 7 in Reynolds et al. (2017).

To characterise the capillary pressure heterogeneity, we use observations obtained at flow regimes far from the viscous limit, where the capillary pressure is the main control on the saturation distribution (Pini and Benson, 2017). For the low flow rate Bunter and Bentheimer experiments, the maximum N_c across the fractional regime is of the order $10^{-1} - 10^0$, below the transition regions identified in Reynolds and Krevor (2015) and Reynolds et al. (2017).

In the following following sections we present the combined experimental and numerical characterisation methods, moving from routine rock properties such as porosity, absolute permeability and viscous limit relative permeability through to capillary pressure heterogeneity and numerical calibration.

2.1. Porosity & absolute permeability

Steady-state core flood experiments are performed using the experimental technique described in detail in Reynolds and Krevor (2015); Reynolds et al. (2017). 3D porosity maps are calculated using medical X-ray CT scanning of the brine saturated rock core through differencing of the saturated image with a dry scan image, in the standard method described in Akin and Kovscek (2003). For the 3D porosity and saturation maps, scans were repeated three times at each step to increase precision; see section 3.2 for a discussion on the error quantification for voxel, slice and core averaged porosity/saturation. Transverse, slice averaged porosity maps of the Bentheimer and Bunter cores are shown in Figure 1, highlighting the homogeneous axial structure of the Bentheimer, and the heterogeneous layering present in the Bunter.

The absolute permeability to brine is calculated at multiple flow rates using the 1D form of Darcy's law applied over the length of the rock core, shown in Table 1. In this characterisation effort, we do not seek to find the 3D permeability map as in previous studies (Krause et al., 2013; Krause and Benson, 2015), since at the sub-metre scale capillary pressure dominates the flow regime (Kuo and Benson, 2013).

2.2. Viscous limit relative permeability

The high flow rate steady-state core flood experiments are used to characterise the viscous limit relative permeability; see Table 1 for details of the experimental conditions. To determine a suitable functional form of relative permeability, the experimental slice average saturation data and pressure drops at each incremental gas fractional flow

are used in a numerical regression scheme in the 1D simulator SENDRA^{TM}. Darcy's law combined with conservation of mass is solved with a given relative permeability parameter estimation, i.e.:

$$\frac{\partial}{\partial x}\left(\frac{-kk_{rj}(S_j)}{\mu}\frac{\partial P_j}{\partial x}\right) = 0 \tag{2}$$

subject to the constitutive relations $P_c = P_g - P_w$ and $S_w + S_g = 1$. Here, j refers to the phase (gas or water), u_j is the velocity, k is the absolute permeability, k_{rj} is the relative permeability, μ_j is the viscosity, P_j is the phase pressure, S_j is the fluid saturation and P_c is the capillary pressure.

With each iterative solution of equation (2) the relative permeability function, $k_{rj}(S_j)$ is varied using a least squares numerical regression to best fit the experimental 1D saturation profiles and pressure drops with the simulated values. A $P_c(S_w)$ function determined from mercury intrusion capillary pressure (MICP) testing (described in section 2.3) is also included in the simulation to take into account boundary effects. Since the fluid saturations in the high flow rate experiments are effectively homogeneous 1D profiles in the central region of the core (see Reynolds and Krevor (2015), Reynolds et al. (2017)), the 1D numerical regression scheme incorporating capillary pressure can accurately derive the viscous limit ('intrinsic') relative permeability.

In this work, we find the Chierici relative permeability functional form the most suitable for our experimental data, due to its versatility and the convex/concave curvatures that are possible (Chierici, 1984). The function is defined by the following equations:

$$k_{rg} = k_{rg}(S_{wirr})e^{-BR_w^M} \tag{3}$$

$$k_{rw} = k_{rw}(S_{gc})e^{-AR_w^{-L}} \tag{4}$$

$$R_w = \frac{S_w - S_{wirr}}{1 - S_{gc} - S_w} \tag{5}$$

where subscript r, g, w, c and irr refer to relative, gas, water, critical and irreducible respectively. The Chierici formulation allows regression of the parameters A, B, M and L to control the shape and curvature of the relative permeability function. Based on the experimental observations of the saturation maps we set $S_{gc} = 0$ for both cores, and $S_{wirr} = 0.0812$ for the Bentheimer and $S_{wirr} = 0.0821$ for the Bunter, discussed in more detail in section 2.3. We also set $k_{rg}(S_{wirr}) = k_{rw}(S_{gc}) = 1$ for both cores. Upon determination of the best fit relative permeability parameters, some manual adjustments are also performed to ensure the curves near the endpoints (which are not reached in the slice average, viscous limit) accurately reproduce the voxel saturations in 3D simulations at lower flow rates. This generally only involves adjusting the gas relative permeability to allow high water saturations to be reached.

The viscous limit relative permeabilities for each core calculated through numerical regression are shown in Figure 2 with the Chierici regression fit parameters detailed in Table 1. The discrete experimental relative permeabilities $k_{r,j}$ in Figure 2 are calculated using core-average saturation data and pressure drops, i.e.:

$$k_{r,j}(S_j) = \frac{q_j \mu_j L}{kA\Delta P_j} \tag{6}$$

where q_j is the volumetric injection rate, L is the core length and A is the core area. Equation (6) generates an equivalent relative permeability, which is an upscaled function incorporating the impact of sub-core scale capillary pressure heterogeneity and any impact of capillary end effects at the inlet and outlet boundaries of the rock sample. It is therefore dependent on both flow rate and the structure and orientation of heterogeneity. In the high flow rate experiments, the equivalent relative permeability coincides with the viscous limit relative permeability, shown in Figure 2. This is expected, since capillary pressure heterogeneity is negligible in the viscous limit, meaning the core-averaged saturations and voxel/slice-averaged saturations are very similar.

In Figure 2, the core average water saturations in the experiments range from 27 - 62%, in which the relative permeability to both gas and liquid remains $k_{rj} < 0.12$. This is typical of core flood experiments using low viscosity fluids where the maximum capillary pressure achievable is limited by the viscous pressure variation between the

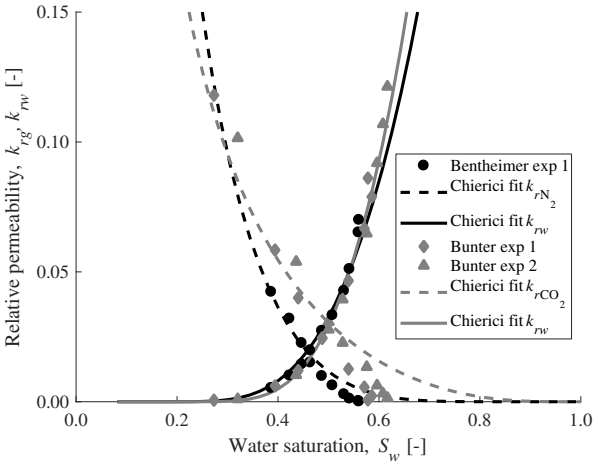

Figure 2: Viscous limit relative permeability of the Bentheimer and Bunter sandstones obtained at high fluid flow rates.

upstream and downstream ends of the rock core (Krevor et al., 2012). The viscous limit relative permeabilities for the Bentheimer and Bunter are similar, which is due to the comparable pore structures indicated by the average capillary pressure curves for the cores, unimodal pore size distribution (Figure 3) and average absolute permeabilities.

2.3. Capillary pressure heterogeneity - the initial estimate

To characterise capillary pressure heterogeneity, we use observations of average capillary pressure characteristics and 3D saturation maps from the core flood experiments, in an iterative numerical calibration process. The observational standpoint is based primarily on the work of Pini and Benson (2013b,a), whereby an initial estimate of capillary pressure heterogeneity can be derived from the observed saturation heterogeneity in steady-state two phase core floods. This information is used in an iterative calibration of a numerical model of the rock core. This builds on the approach of Krause (2012); Krause et al. (2013); Krause and Benson (2015) by incorporating multiple fractional flows and total flow rates into the iterative calibration. Distinct from past studies, we then make use of the numerical model in the derivation of equivalent relative permeability.

In order to determine the capillary pressure heterogeneity, we use a combination of MICP experiments, 3D experimental saturation maps and numerical calibration. Small core samples are drilled from the larger rock cores after steady-state core flooding for use in MICP testing to obtain capillary pressure curves which are representative of the average curve for the whole core. Figure 3 shows the MICP data which has been scaled by interfacial tension to represent the appropriate fluid pairs used in the experiments, along with fitted Brooks-Corey curves with parameters detailed in Table 1. We use the Brooks-Corey model for capillary pressure P_c in this work, due to its applicability over a wide range of porous media systems (Pini and Benson, 2013b):

$$P_c(S_w) = P_e \left(\frac{1 - S_{wirr}}{S_w - S_{wirr}} \right)^{1/\lambda} \tag{7}$$

where, P_e is the entry pressure, S_{wirr} is the residual water saturation and λ is the pore-size distribution factor.

We use the threshold pressure of the uni-modal rock cores (see the pore size distributions in the inset of Figure 3) measured in the MICP experiments as the representative entry pressure for the average system. To determine S_{wirr}, the steady-state 3D saturation from the core flood is used to infer the highest residual that could possibly be achieved. By sampling the MICP data above this point, the Brooks-Corey model can then be determined by minimising the fit between the MICP data and predicted $P_c(S_w)$ through variation of λ and S_{wirr} with fixed P_e. The parameters obtained from this fitting process are shown in Table 1, with the corresponding curves shown in Figure 3.

Saturation maps from the low flow rate experiments are used as the principal information to obtain an initial estimate of the 3D capillary heterogeneity (Egermann and Lenormand, 2005; Pini et al., 2012; Pini and Benson,

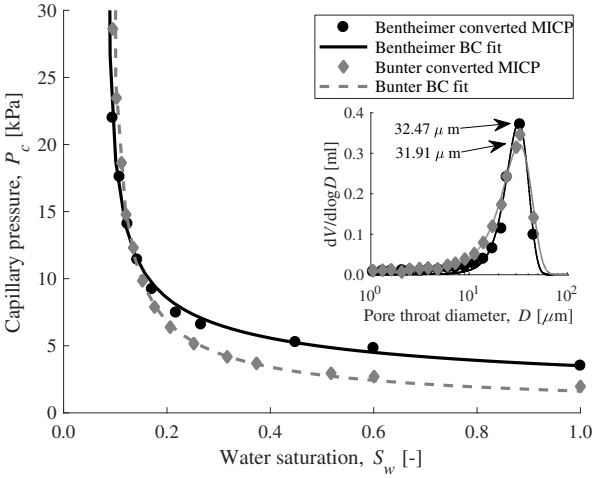

Figure 3: Mercury intrusion capillary pressure data for Bentheimer and Bunter micro-cores, drilled from the main cores. The data is converted to the respective fluid pairs used in the experiments. Brooks-Corey capillary pressure curves are fitted to the experimental data points through optimisation of λ and S_{wirr}. The inset shows the pore size distribution data from the MICP experiment.

2013a; Krause et al., 2013; Reynolds and Krevor, 2015). 3D voxel saturation (and porosity) maps are calculated by arithmetically upscaling the high resolution X-ray scan data, to improve the precision (discussed in section 3.2) and to ensure that the voxel size is above the minimum REV needed for Darcy's law to be applicable on the continuum scale. See Zhang et al. (2000); Fernandes et al. (2012); Pini and Madonna (2016) for discussion of the REV for various sandstones. We upscale the raw scan resolution by a factor of 8x8x1 in the x-y-z directions, to achieve voxel sizes above the REV for permeability & porosity in sandstone cores, see Table 1.

To relate the experimental saturation to individual capillary pressure curves in each voxel, the average Brooks-Corey capillary pressure curve is used as a base. As an initiating guess in the calibration process, we assume the capillary pressure in each transverse slice of the core is constant as in Krause et al. (2013); Krause and Benson (2015). Under this assumption, the average saturation in each transverse slice can be mapped directly to the average Brooks-Corey capillary pressure curve. The variation in saturation of individual voxels within the slice gives an indication of the spatial heterogeneity in the capillary pressure characteristic. The variation in capillary pressure from the average Brooks-Corey curve for each voxel i is then given by a unique scaling factor κ_i:

$$P_{c,i}(S_i) = \kappa_i \tilde{P}_c(S_i) \tag{8}$$

where S_i is the water saturation at voxel location i, $\tilde{P}_c(S_i)$ is the average characteristic capillary pressure and $P_{c,i}(S_i)$ is the individual voxel capillary pressure. The scaling parameter κ_i is initially obtained directly from the experimental data following the approach of (Pini and Benson, 2013a, 2017). For each fractional flow, the slice average saturations $\tilde{S}^{exp}$ are mapped to the average Brooks-Corey curve to find the slice average capillary pressures $\tilde{P}_c$ with corresponding voxel saturations S_i^{exp}. From this, κ_i can be used to scale the average capillary pressure $\tilde{P}_c(S_{ij}^{exp})$ to the individual voxel capillary pressures $P_{c,i}(S_{ij}^{exp})$ at each fractional flow j, through minimisation of the following objective function:

$$\Phi = \sum_i^{N_v} \sum_j^{N_f} \sqrt{\left(\kappa_i \tilde{P}_c(S_{ij}^{exp}) - P_{c,i}(S_{ij}^{exp})\right)^2} \cdot \sqrt{\left(S(\kappa_i \tilde{P}_c = \tilde{P}_c(\tilde{S}_j^{exp})) - S_{ij}^{exp}\right)^2} \tag{9}$$

where N_v is the total number of voxels, N_f is the total number of fractional flows, $\tilde{P}_c$ is the average Brooks-Corey curve and $\tilde{S}_j^{exp}$ is the slice average saturation containing the voxel saturation S_{ij}^{exp}. $S(\kappa_i \tilde{P}_c = \tilde{P}_c(\tilde{S}_j^{exp}))$ refers to the saturation predicted with the new curve $\kappa_i \tilde{P}_c$ at the slice average capillary pressure and saturation $\tilde{P}_c(\tilde{S}_j^{exp})$.

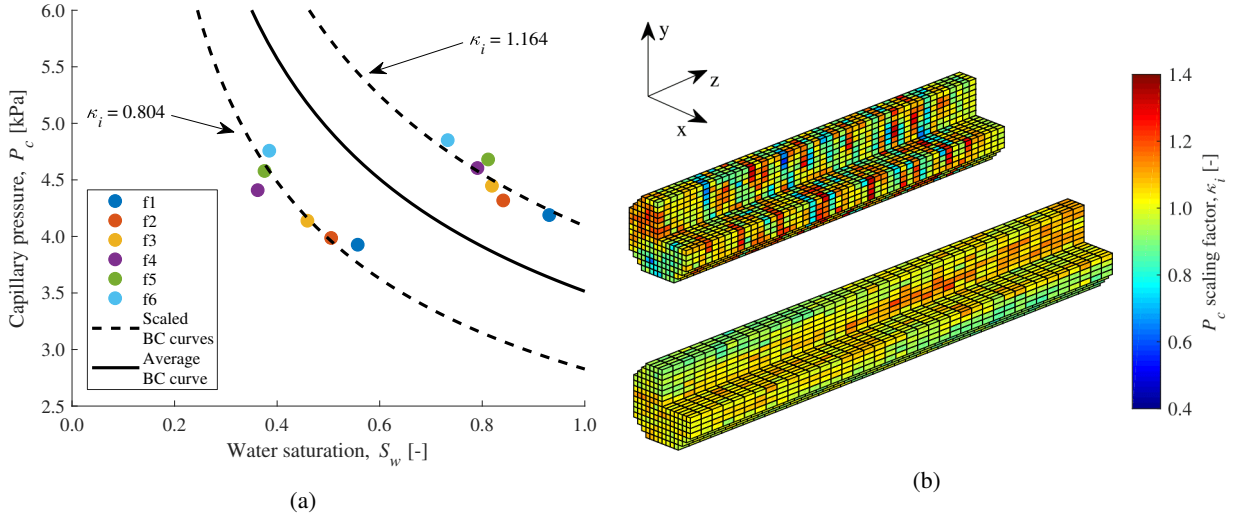

Figure 4: (a) Scaling factor κ_i for two voxels in the Bentheimer core found through the minimisation of equation (9). (b) Maps of κ_i in the Bunter (top) and Bentheimer (bottom) sandstone cores, obtained from the initial experimental characterisation. Rock core coordinate system shown in the top left corner of (b).

We minimise both the predicted capillary pressure and saturation with κ_i so that we minimise the effective distance between the predicted curve and the individual $P_c(S)$ points. This also helps to normalise the minimisation so that points at the extremes of the curves have similar weightings to central points, rather than adversely affecting the weighting using a relative error function.

The minimisation process is applied to all voxels, resulting in a 3D map of the scaling factor κ_i for each core. With this, an initial approximation to the capillary pressure heterogeneity in the core can be obtained, shown in Figure 4b. This initial estimate already highlights the capillary layering that is present in both cores with variations $\Delta\kappa_i \approx 0.5$ resulting in ΔP_e between layers of around 1-1.5kPa, which would appear 'homogeneous' in single phase tracer tests (Reynolds and Krevor, 2015). In the Bentheimer core, there is a high entry pressure layer parallel to the principal flow direction (z-axis), more prominent at the downstream end of the rock core than in the upstream end. In the Bunter sandstone, there are repeated layers oblique to the z-axis, some of which pinch out against the confining sleeve holding the rock core.

The initial assumption of a constant capillary pressure (in each slice or across the whole core) is not strictly valid for heterogeneous cores in core flood experiments (since $\nabla P \neq 0$). While we require this assumption to gain an initial approximation of the heterogeneity, it can be relaxed using numerical calibration in order to derive the true, unique capillary pressure heterogeneity (Krause, 2012; Krause et al., 2013). Through the numerical simulation of the low flow rate core flood experiments, we can assess the validity of the 3D capillary pressure representation using the simulated and experimental fluid saturations. The capillary pressure heterogeneity can then be updated to obtain a more representative distribution inside the core, allowing greater characterisation of the multiphase flow properties.

2.4. Capillary pressure heterogeneity - iterative calibration of the numerical model

We represent the rock core numerically using an orthogonal, Cartesian mesh with cells of the same dimension as the voxels obtained from the upscaled experimental observations, resulting in a grid $14 \times 14 \times 39$ for the Bentheimer, and $14 \times 14 \times 49$ for the Bunter. Specific outer cells are removed to create the cylindrical core with a total of 6708 and 8428 cells for the Bentheimer and Bunter models respectively. The numerical core diameters are smaller than the physical cores to alleviate any scanning or upscaling artefacts that can appear near the outer circumference of the cores. The superficial Darcy velocity through the inlet face of the core (Q_{tot}/A) is maintained at the same level as the experimental core by adjusting the volumetric flow rate Q_{tot} accordingly.

The CMG IMEX^{TM} fully implicit, isothermal immiscible multiphase porous media flow simulator is used to numerically simulate the core flood experiments. 3D multiphase Darcy's law is solved along with conservation of

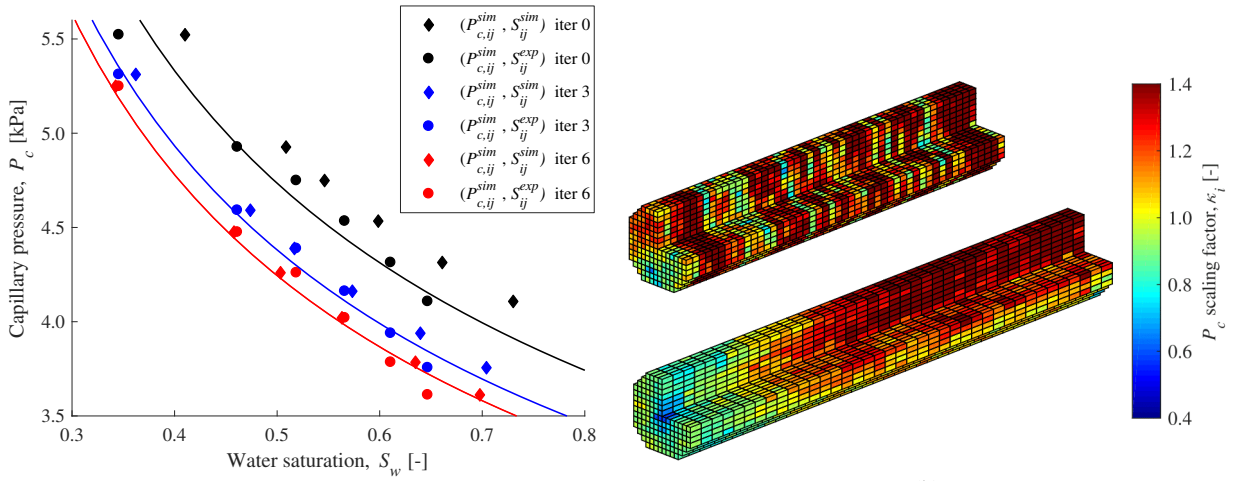

(a) (b)

Figure 5: (a) An example of the iterative capillary pressure calibration scheme using the experimental voxel saturations and simulation capillary pressures for a voxel in the Bentheimer core. Solid lines are the resulting Brooks-corey curves at each iteration with optimised κ_i, found from the minimisation of equation (10). (b) κ_i map for the Bunter (top) and Bentheimer (bottom) cores after 6 iterative calibrations using equation (10).

mass and constitutive equations for the gas-liquid saturations and capillary pressures. The system of equations are discretized into finite-difference form using first order backward differences in time, and central differences in space with upstream mobilities.

Fictitious inlet and outlet boundary slices are used to enforce the boundary conditions of the system. There has been significant discussion on appropriate boundary conditions that should be used for the analytical and numerical simulation of core floods (see Krause (2012) for a thorough review), in which the discontinuity in capillary pressure at the core end caps is difficult to prescribe for multiphase porous media simulation. In the physical experimental end caps, there is a single inlet port which contains the fractional mix of injection fluids, a pressure transducer tap, and a spiral groove in the end cap, designed to spread the fluids evenly onto the inlet face of the core. Regardless of the grinding and sanding of the inlet face of the core, there is always some small gap, usually under 1mm between the core face and the end cap. In the numerical simulation in this work, we use the fictitious slices to model this small gap, where the boundary conditions can be fairly well approximated; there is zero capillary pressure and the fluid saturation is controlled solely by gravity and the fractional flow. In the numerical model, we therefore use a very large permeability ($> 10D$), constant porosity, linear relative permeability and zero capillary pressure.

We choose not to alter the capillary pressure of the outlet slice for each fractional flow as in Krause et al. (2013), as we do not wish to bias the calibration by imposing a non-physical boundary condition. By using the same boundary condition for all fractional flows across all flow rates, we ensure that the capillary pressure calibration is only affected by the experimental saturations. We can then judge the boundary affected region by comparing directly with experiment, and in further simulations outside of the tested fractional regimes we can simply remove the affected regions and the boundary effects all together, ensuring only the accurately calibrated region is used.

To represent the injection of fluids into the system, we use injection wells in the CMG IMEX format. Two wells are used for each fluid component injection which are completed in the central 2x2 voxels in the inlet slice, creating a constant flux inlet boundary condition. Two constant pressure wells are used in the outlet slice to create a constant pressure outflow boundary condition. The rock-fluid properties in Table 1 are used as inputs to the simulator; average properties are assigned to the whole core, whilst the 3D porosity and capillary pressure scaling factors are defined for each grid cell. Each simulation runs for the same period of time as the steady-state core flood experiments, i.e. at each fractional flow at least 5-10 pore volumes of fluid are injected to allow the system to reach steady-state.

To calibrate the 3D capillary pressure heterogeneity in the core, we build on the works of Krause (2012) and Krause et al. (2013) by extending the iterative approach to multiple fractional flows and flow rates, operating solely on the capillary pressure. The calibration procedure uses as a guiding principle that 3D saturation information is

most accurately obtained from the observations, whereas the associated capillary pressures for each location are most accurately obtained from the numerical simulation. A difference between observed and simulated saturation at a given location is then due to an incorrect scaling of the capillary pressure curve at that location. After each simulation iteration we produce a capillary pressure - saturation pair at each fractional flow, which we update with the experimental saturation, i.e. ($P_{c,ij}^{sim}$, S_{ij}^{sim}) becomes ($P_{c,ij}^{sim}$, S_{ij}^{exp}), shown in Figure 5a. These updated points are then used in a minimisation process to find the new κ_i to scale the average Brooks-corey curves, in a similar fashion to the original experimental scaling in equation (9):

$$\Phi = \sum_{i}^{N_v} \sum_{j}^{N_f} \sqrt{\left(\kappa_i \tilde{P}_c(S_{ij}^{exp}) - P_{c,ij}(S_{ij}^{sim})\right)^2} \cdot \sqrt{\left(S(\kappa_i \tilde{P}_c = P_{c,ij}(S_{ij}^{sim})) - S_{ij}^{exp}\right)^2} \tag{10}$$

where the slice average capillary pressures have been replaced by the simulation capillary pressure at the voxel scale, $P_{c,ij}(S_{ij}^{sim})$, and the saturations we minimise towards are the experimental voxel values, S_{ij}^{exp}. Using the above minimisation, the experimental voxel saturation and simulated capillary pressure are used to update the scaling factor κ_i in an iterative fashion. The minimisation was performed using a single fractional flow in Krause et al. (2013) and is extended in this work to multiple fractional flows. Using multiple fractional flows reduces systematic error from calibration bias, discussed in more detail in section 3.2.

An example of the iterative calibration scheme for a single voxel using all 6 fractional flows in the low flow rate Bentheimer core flood is shown in Figure 5a. With each each iteration, the low flow rate core flood experiment is simulated with the numerical model and the resulting voxel capillary pressures $P_{c,ij}^{sim}(S_{ij}^{sim})$ and experimental saturations are used in the minimisation equation (10). From this, a new κ_i is generated for each voxel, which can be updated in the simulation, and the process reapeated. Upon iterative calibration of the capillary pressure curves, the simulation voxel saturations converge to the experimental values, with each iteration improving the result. The calibration is completed when the mismatch between the observations and simulation no longer improves, or improves marginally (i.e. less than 1%) with further iteration.

Calibration of the capillary pressure heterogeneity completes the experimental characterisation effort, after which the rate invariant, intrinsic rock properties which describe isothermal, immiscible multiphase flow at the mm scale have been characterised. We now analyse the accuracy and robustness of the characterisation by simulating the low flow core flood experiments with the numerical models, and comparing the predicted relative permeabilities to those found experimentally. Both the base case experimental characterisation, and the iterative numerical calibration are compared in the following result sections.

3. Results & discussion

3.1. Calibration results based on the initial estimate of capillary heterogeneity

First we evaluate the extent to which the model calibrated through the initial guess, without iteration, recreates the experimental observations. The low flow rate core flood experiments can be numerically simulated and the equivalent relative permeability calculated using the multiphase extension to Darcy's law, equation (6). The simulated equivalent relative permeabilities give a direct indication of the accuracy and predictability of the numerical model when compared to the experimentally derived values.

Results of the numerical simulations for the Bentheimer and Bunter cores using the initial experimental characterisation are shown in Figure 6. The R^2 values of 0.48 and 0.31 for the Bentheimer and Bunter respectively highlight a weak but statistically significant correlation between the simulation and experiment saturations. The transparent scatter points in the plots are points that lie outside the central 5/7ths of the cores, representing voxels that are likely to be affected by discrepancies between how the simulation represents end effects and the physical experiment. In the Bentheimer core, the voxels near the boundaries show significantly more scatter than the central voxels of the core, whereas the discrepancy is more uniformly distributed throughout the more heterogeneous Bunter sandstone.

The tailing of the low simulations saturations in the Bentheimer core is largely due to the capillary entry pressure at the outlet of the core, which is too small in simulation compared to what is physically occurring in the experiment. At very low gas saturations, there is very little information regarding the capillary pressure, since the pore space is

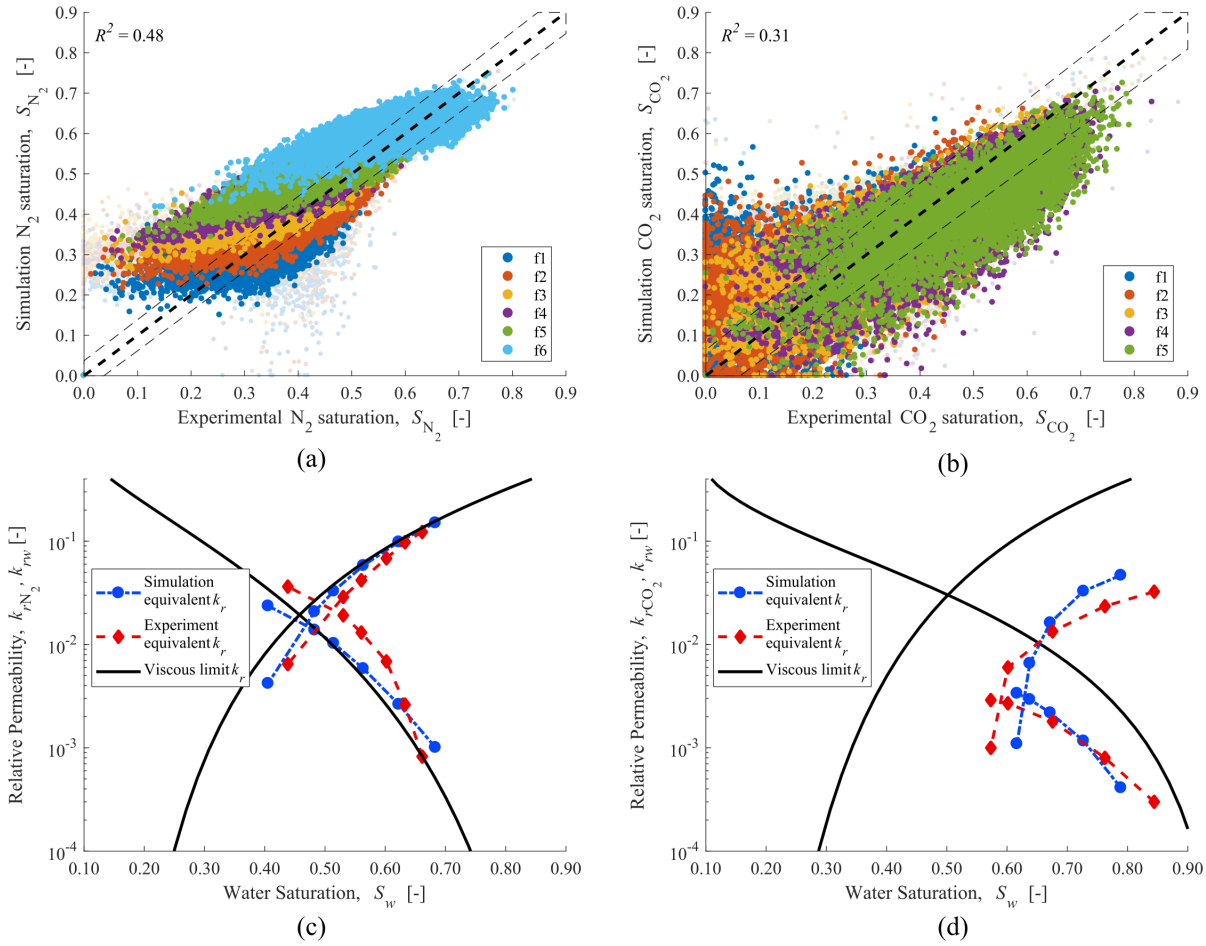

Figure 6: Results from numerical simulations using rock properties derived purely from the experimental characterisation effort. (a)-(b) Simulation and Experiment voxel saturation scatter plots for the Bentheimer & Bunter respectively. The dashed lines bound the uncertainty ($\pm 2\sigma$) in the experimental voxel saturations. (c)-(d) Equivalent relative permeability in the low flow rate regimes for the Bentheimer & Bunter respectively.

almost entirely occupied by water. This means the scaling of the average capillary pressure curve is not as significant as it should be, and the entry pressure is under-predicted. This effect can be seen towards the outlet of the core in Figure 7a, where the gas saturation approaches zero, and the lack of capillary pressure scaling information has resulted in an under-predicted entry pressure in this region.

Inlet boundary effects also affect the Bentheimer saturation plot, shown by transparent scatter points in Figure 6a at $S_{\text{exp},N_2} \approx 0.3-0.5$, which are under-predicted by the simulation. This is mainly due to gravity segregation occurring at the inlet of the core in the simulation, due to the homogeneous, large permeability of $2.2D$, seen in the top left of the saturation plots in Figure 7a. Since only the average absolute permeability parallel to the flow direction is measured, it is possible that the transverse permeability is lower in the experiment and hence why there is little segregation in the experimental saturations.

It is clear from saturation plots that the Bunter has an increased capillary pressure heterogeneity compared to the Bentheimer, resulting in a greater spread of saturations around the identity line. However, the points do spread largely symmetrically over the identity line, indicating that the prediction is not biased towards certain gas saturations, and that the scheme is equally effective across the whole saturation range. The Bunter also does not show any significant boundary effects, partially due to the much lower flow velocity being simulated, but also due to the perpendicular capillary layering, which causes build-up of CO_2 saturation behind areas of high capillary entry pressure. This limits

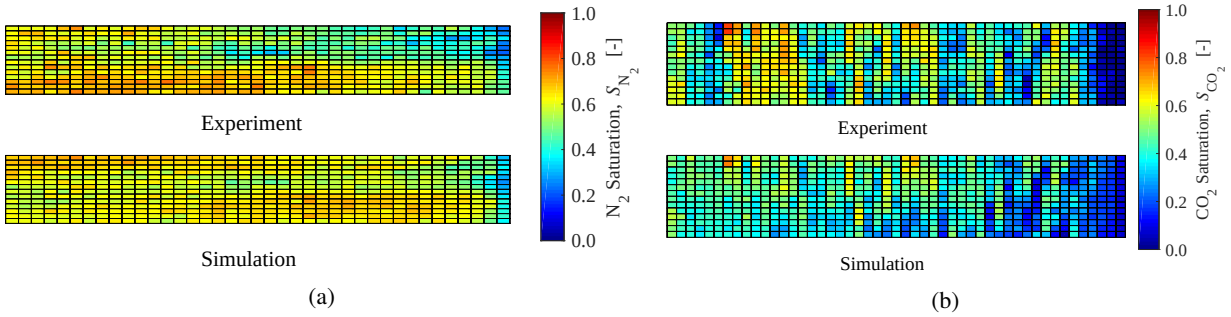

(a) (b)

Figure 7: Voxel saturation maps of a central slice from the cores taken in the y-z plane parallel to the flow direction (a) Bentheimer fractional flow 6, $f(N_2) = 0.9929$. (b) Bunter fractional flow 5, $f(CO_2) = 0.975$.

the impact of the $P_c = 0$ discontinuous end slice and also reduces gravity segregation by compartmentalising the CO_2 into separate regions, shown in Figure 7b.

The equivalent relative permeabilities at low flow rate predicted by the simulation are shown in Figures 6c and d. In both plots, the predicted relative permeabilities are close to the experimentally derived values, exhibiting similar curvatures and endpoints, with any discrepancy mainly in the form of saturation error.

For the Bunter, both the gas and water predicted equivalent relative permeability drop below the viscous limit values, as in the experiments. A significant reduction in the gas or non-wetting phase relative permeability curves is common for perpendicular layered systems at low flow rate (Rabinovich et al., 2016; Virnovsky et al., 2004), where wetting phase relative permeabilities are also lowered, albeit not for the entire saturation range. The water relative permeability is also reduced, as with the parallel layering. In the case of perpendicular layering, the barriers to flow impact both fluid phases.

In the Bentheimer in Figure 6c we see a different effect, whereby the equivalent gas permeability is raised at high water saturations. The layering parallel to the principle flow direction allows for the fluid phases to organise themselves more optimally into high and low entry pressure regions. This has the overall effect of boosting the equivalent relative permeability to the non-wetting phase as it flows primarily through regions of locally high N_2 saturation. This effect has also been reported before in previous work (Krause and Benson, 2015; Reynolds and Krevor, 2015; Rabinovich et al., 2016). The increased relative permeability manifests most significantly at lower fractional flows whereby the small amounts of nitrogen injected move preferentially through the low capillary pressure layers, greatly affecting the relative permeability.

The simulated Bunter equivalent relative permeability at low capillary number is quantitatively much more accurate than the Bentheimer when compared to their respective experimental results. The RMS relative errors encompassing both core average pressure drops and saturations are 14.9% and 24.1%, respectively. Since the layering in the Bunter is larger in magnitude compared to the Bentheimer (see Figure 4b) the initial scaling is less sensitive to variance or systematic error. The low flow rate experiment in the Bunter sandstone occurs in a more capillary dominated regime than the Bentheimer, $N_c \approx 0.5$ compared to $N_c \approx 1.5$, respectively. The initial capillary equilibrium scaling assumption is therefore more applicable, and hence more effective for the Bunter flow regime.

From the base results with the initial guess for the characterisation of capillary heterogeneity, the saturation and capillary heterogeneity are slightly under-predicted. This under-prediction is largely due to the initial assumption of a slice averaged, constant capillary pressure. In the next section, we relax this assumption using the iterative calibration method, and analyse the improvement in predictive ability.

3.2. Results from the iterative calibration

The numerical models are calibrated using the simulated capillary pressure and experimental saturation data from the low flow rate core floods as described in 2.3. We present results using numerical calibration, incorporating all fractional flow flows, and with calibration using only one fractional flow as in Krause et al. (2013), to demonstrate the impact of calibration bias.

Saturation maps for the Bentheimer core simulated using the different calibration schemes are displayed in Figure 8. The iterative calibration using all the available experimental data in Figure 8b shows the highest correlation with

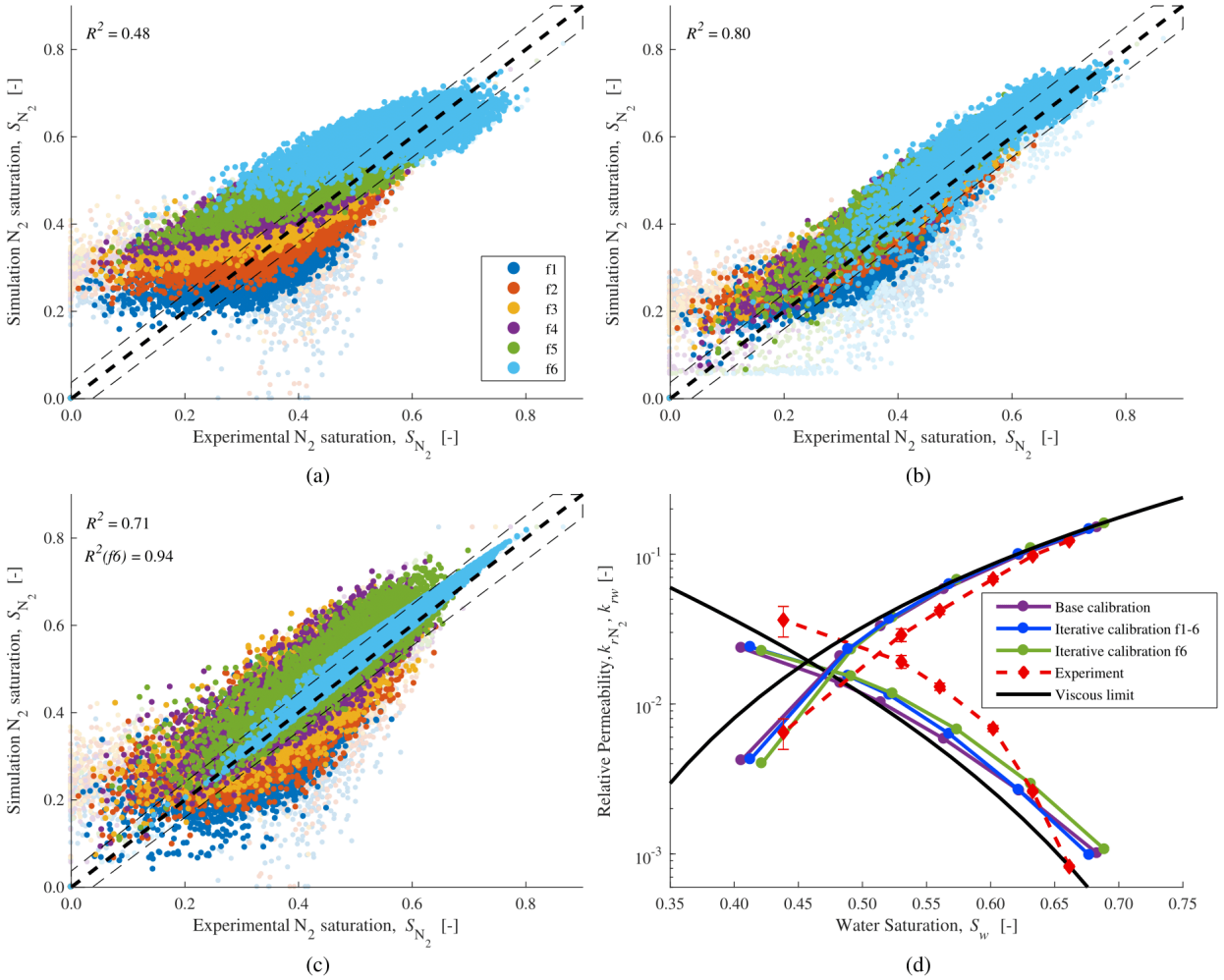

Figure 8: Voxel saturation scatter plots between simulation and experiment using the different calibration schemes. (a) Base case, using the initial experimental characterisation without numerical calibration. (b) Iterative numerical calibration using fractions 1-6 to minimise equation (10) (c) Iterative numerical calibration using only fraction 6 to minimise equation (10). (d) Equivalent relative permeability of the Bentheimer core at low flow rate using the different calibration schemes. Iterative calibration results are shown after 6 iterations

experimental data. Since the scheme uses capillary pressure information across all the fractions that were experimentally tested, it accurately predicts the saturation across the whole range of experimental conditions. The spread of points has decreased significantly from the base case in Figure 8a, and there is also a less prominent tailing where the saturation is close to zero.

In the iterative numerical calibration, the boundary effects present in the Bentheimer have not been significantly reduced, and still appear as outliers in Figure 8b. Since boundary effects are not caused by incorrect voxel capillary pressure curves, calibration using the experimental saturation does not improve the prediction. This is actually beneficial, since incorrectly modelling the boundary conditions with variations in capillary pressure heterogeneity would reduce the overall predictive ability of the scheme. Calibrating using additional experimental data also helps to reduce the uncertainty associated with boundary effects, since not all fractional flows are equally affected, meaning a particular fractional does not completely bias the calibration.

The iterative calibration approach with a single fractional flow ($f6$), analogous to that presented in Krause et al. (2013), is shown in Figure 8c. The calibration has resulted in a near perfect correlation between the simulated and experimental voxel saturations for $f6$, with almost all voxels lying within two standard deviations of the experimental error (dashed box around the identity line). The overall correlation considering all fractional flows has also improved

from the base case, as the calibration using $f6$ still captures much of the underlying information associated with the capillary pressure heterogeneity. Although near perfect correlations can be obtained when calibrating to high gas fractional flows, the iterative approach does not perform as well when calibrated against an observation at low fractional flow. At low fractional flows, more voxels have saturations close to zero, meaning there is less information to update the capillary pressure curves and the iterative scheme converges very quickly to a result no better than the base case.

The predicted low capillary number equivalent relative permeability curves for each different calibration scheme can be seen in Figure 8d for the Bentheimer. The iterative calibration schemes have improved the prediction over the base case, largely due to a better prediction of the core average saturation, with predicted pressure drops remaining fairly similar. The iterative calibration using all fractional flows shows the best match with experiments across the tested saturation range, particularly at high water saturations. Although differences are seen in the gas relative permeability curves, the water curves remain very similar. The decrease in water relative permeability in the experiment is likely caused by the boundary conditions (discussed in more detail in section 3.4), which all schemes model with $P_c = 0$. Since the outlet boundary condition is not explicitly calibrated, we see the same behaviour with all the iterative schemes; a slight under-prediction of the water saturation towards the outlet of the core.

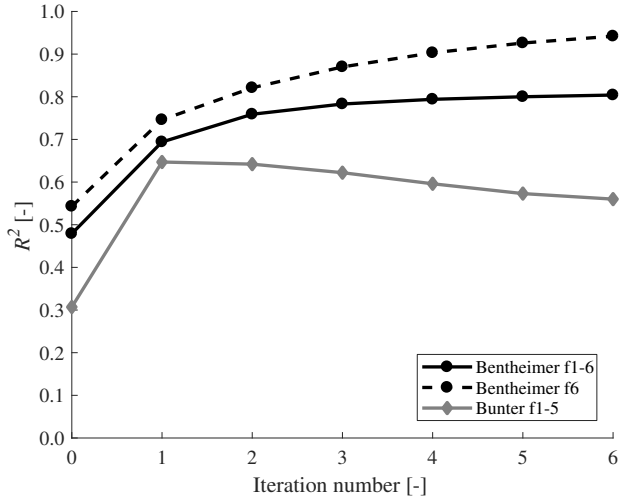

Figure 9: R^2 values between experiment and simulation voxel saturations for each iteration of the iterative calibration schemes. The zeroth iteration refers to the base case using purely experimental characterisation.

The convergence of the iterative calibration schemes can be seen in Figure 9. After 5-6 iterations, the calibration schemes using all fractional flows effectively converge to a constant R^2, validating that the final solution is not subject to further changes with iteration. The $f6$ calibration scheme has yet to converge in Figure 9, and only converges after 10 iterations, when $R^2(f6) \rightarrow 1$.

The iterative calibration scheme is applied to the Bunter core, using the experimental saturation data from the 5 low flow rate fractional flows. Figure 10a shows the resulting simulation saturations after 6 calibration steps compared to the experimental data. The saturation deviation of the high fractional flows has been drastically reduced when compared to the base case in Figure 6, with most voxel saturations from $f3-5$ falling within the experimental precision. The lower fractional flows show a systematic increase in CO_2 saturation towards $S_{CO_2} = 0$, compared to the experimental values. This trend is due to the capillary entry pressure which has been under-estimated at the low fractions, where $S_w \approx 1$ in many voxels. Since the flow rate of CO_2 is only 0.02 ml.min^{-1} for $f1$, many of the high entry pressure voxels remain at $S_w = 1$. The entry pressure is not scaled enough for these voxels, since the low fractional flow saturation provides little information towards the minimisation process in equation (10), with the higher fractional flows biasing the result. Incorporating further information for improved $S_w = 1$ voxel scaling is the feature of on-going research, and is beyond the scope of the current work.

The prediction of the low capillary number equivalent relative permeability is shown in Figure 10b. The improved correlation between simulation and experimental saturations using the iterative calibration has enhanced the relative

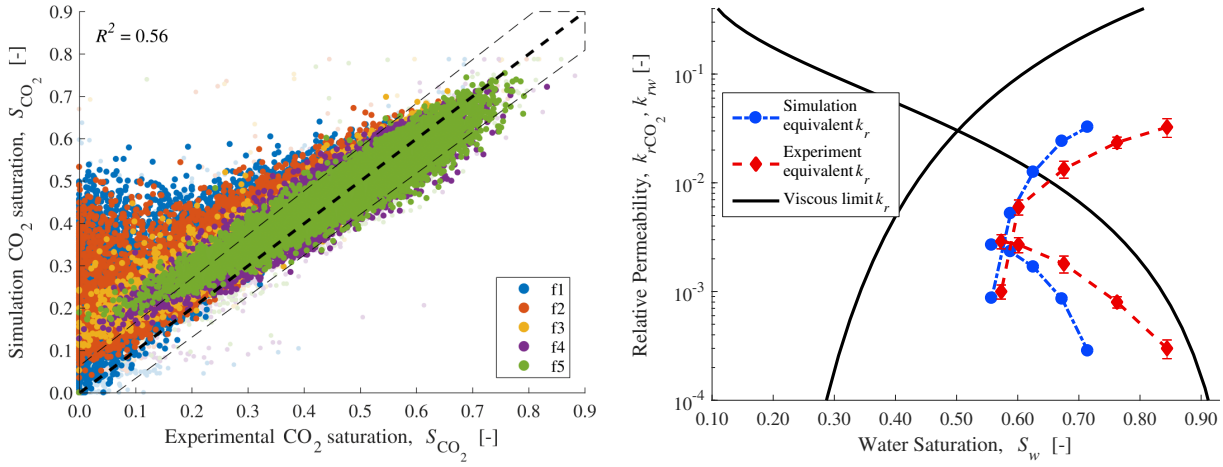

(a) (b)

Figure 10: (a) Voxel saturation scatter plot between simulation and experiment using the iterative calibration across all fractions for the Bunter core. (b) Corresponding equivalent relative permeability for the Bunter at low flow rate.

Uncertainty	Bentheimer	Bunter
$\sigma_{S,vox}$ [-]	0.0185 - 0.0262	0.0321 - 0.0454
$\sigma_{S,slice}$ [-]	0.0011 - 0.0016	0.0061 - 0.0086
$\sigma_{S,core}$ [-]	0.0002 - 0.0003	0.0009 - 0.0012
$\sigma_{\Delta p}$ [kPa]	0.4595 - 0.7676	0.2012 - 0.3131

Table 2: Experimental saturation uncertainty from voxel to core scale and pressure drop uncertainty in the from of variance error.

permeability prediction, especially at low S_w saturations, with the curvature of both CO_2 and brine relative permeabilities accurately captured by the simulation. The pressure drops and resulting relative permeabilities predicted by the simulation are within the experimental errors, shown in Figure 10b, although the average saturation is most accurate for the higher fractional flows.

The prediction of the Bunter relative permeability at low flow rate highlights the effectiveness of the capillary pressure calibration, and the predictive qualities of the numerical model. At this point, it is worth discussing the experimental precision, and the effect this has on the resulting calibration efforts. The saturation precision at various levels of upscaling, along with pressure drop uncertainty is detailed in Table 2. The saturation uncertainty is calculated using the techniques described in (Pini et al., 2012; Pini and Madonna, 2016), based on the standard deviation of CT numbers obtained upon subtraction of two dry-scan medical X-ray images. The voxel level uncertainty in saturation ranges from 3.21 - 4.54% for the Bunter and 1.85% - 2.62% for the Bentheimer, which is achieved through 8x upscaling of the raw scan resolution, 3x averaging of independent scans and a large z-axis slice thickness used for each scan. Upon further upscaling to the slice or core level, the saturation precision is improved significantly. The pressure error in Table 2 is shown graphically in the form of relative permeability uncertainty in Figures 8d and 10b ($2\sigma_{\Delta p}$ shown), whereby the errors lie largely within the data points.

Due to the high level of experimental precision in the saturation and pressure drop measurements, the uncertainty in the capillary pressure calibration is reduced to that resulting from systematic error. The main contributor of this error is likely the assumption of capillary pressure equilibrium which is the basis of the calibration efforts. We initially assume that the average saturation maps directly to capillary pressure, with changes in capillary entry pressure causing a corresponding change in local saturation.

The validity of this assumption can be assessed by comparing the Bentheimer and Bunter simulation results. The pressure and core-average saturations are predicted significantly better by the Bunter model, despite larger relative variance errors in the saturation and pressure data. The RMS relative error is 9.8% and 18.7% for the Bunter and Bentheimer respectively, after 6 calibration iterations. Since the low flow rate regime for the Bunter lies closer to the

limit of capillary equilibrium, the calibration of the capillary pressure curves is more effective, and a closer match can be obtained to the experiments. Lowering the experimental flow rate further would likely improve the calibration method, leading to enhanced characterisation.

Next, we explore the possibility of calibrating the model based on observations obtained at one flow rate.

3.3. The effectiveness of single flow rate characterisation

Thus far, the characterisation of multiphase flow properties in heterogeneous cores has been achieved using experimental data across multiple flow rates and fractional flows. This is the most effective and robust way to characterise heterogeneous cores, since the viscous limit relative permeability and capillary pressure heterogeneity are most accurately derived in distinct flow regimes; viscous and capillary dominated respectively. However, practically, it is beneficial to only perform a single experiment, and characterise the core completely using a single flow rate dataset. With this in mind, we investigate the effectiveness of characterising the numerical models using data solely from the high flow rate experiments.

In the high flow rate experiments, N_c is generally above the transition region for capillary-viscous dominated flow, however, there is still some level of heterogeneity in the 3D saturation maps, which can be used to infer capillary pressure heterogeneity. We therefore use the saturation information from the high flow rate experiments to characterise the capillary pressure, and use the resulting numerical model in a fully predictive way to calculate the low flow rate equivalent relative permeability.

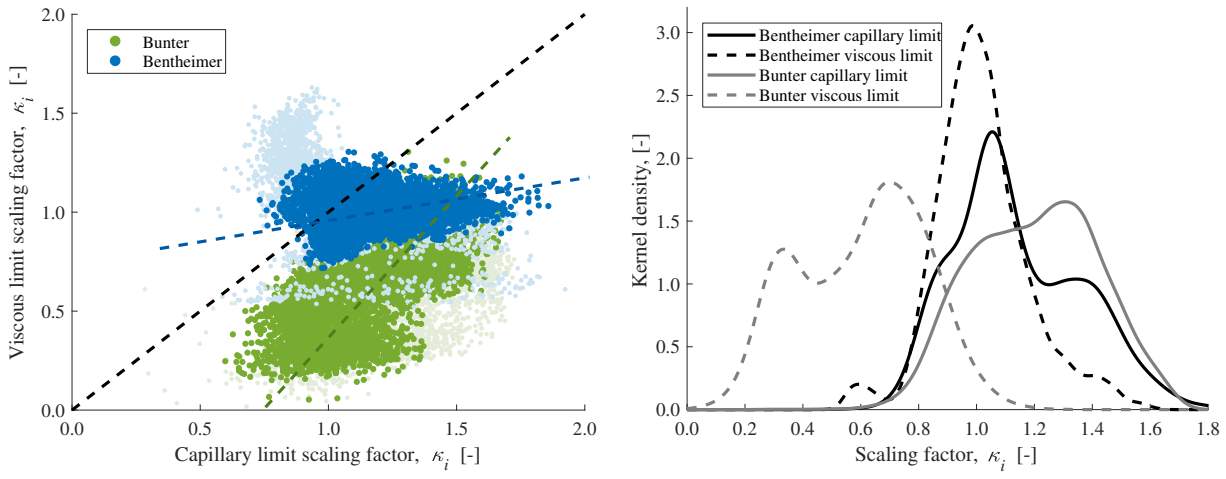

(a) (b)

Figure 11: (a) Comparison of the scaling factor κ_i calculated using high flow rate (viscous limit) experimental data, and low flow rate (capillary limit) data. Dark points are the central 5/7ths of each core. Dashed blue and green lines show the correlation trends for the Bentheimer and Bunter respectively. (b) Density functions of the scaling factor κ_i through the entire core, calibrated using high flow rate (viscous limit) and low flow rate (capillary limit) experimental data. Non-parametric normal kernel density functions are used to estimate the density function of κ_i.

We use fractional flows 6-10 and 5-8 from the high flow rate Bentheimer and Bunter experiments respectively to iteratively calibrate the capillary pressure, since these fractions provide the most information regarding the scaling of the capillary pressure curves, and cover a wide range of saturations. As the high flow rate experiments were also used to derive the viscous limit relative permeability, the equivalent relative permeability predicted at the high flow rate including capillary pressure heterogeneity falls on top of the viscous limit values, with whole-core voxel saturation R^2 values of 0.75 and 0.59 for the Bentheimer and Bunter respectively, when compared to experimental saturations.

The calibrated scaling factors κ_i for the cores using the high flow rate and low flow rate experimental data are shown as a voxel by voxel comparison in Figure 11a. Viscous and capillary limit are used to refer to the calibration using high and low rate data respectively, to indicate the flow regimes that the datasets lie closest to. Both iterative calibration scheme results are shown after 6 iterations with their respective experimental data. In Figure 11a, the Bunter shows a correlated, but systematically lower κ_i prediction using the high flow rate experimental data. The

Bentheimer shows less correlation, however, the majority of points also lie under the identify line, being under-predicted. The transparent points in the plot are the inlet and outlet 2/7ths of the core, and show significantly worse correlation between the two calibration methods due to previously discussed boundary effects.

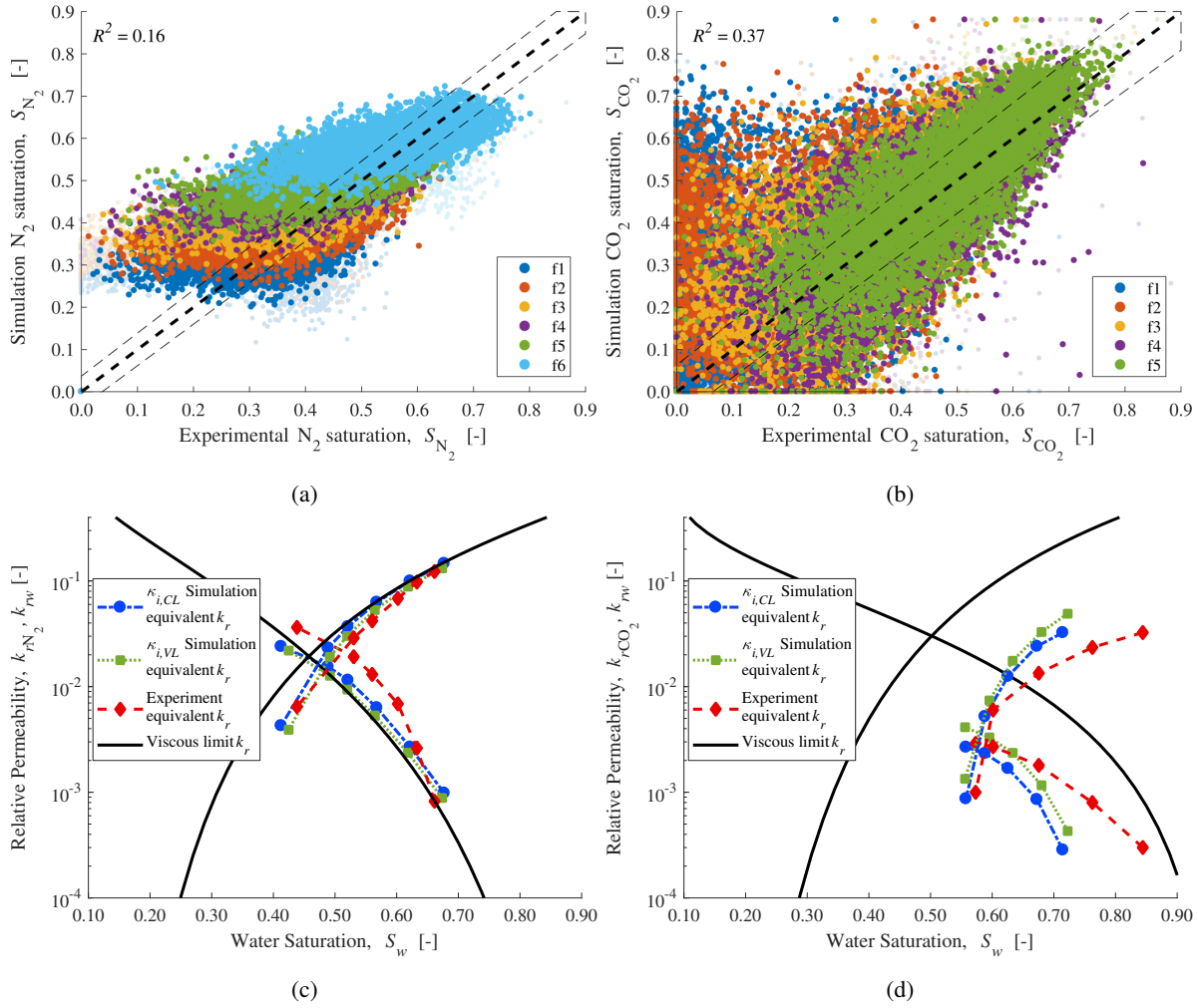

Figure 12: Results from numerical simulations using the capillary pressure scaling factor κ_i calibrated using only the high flow rate (viscous limit) experimental data. (a)-(b) Simulation and experimental voxel saturation scatter plots for the Bentheimer and Bunter respectively. (c)-(d) Equivalent relative permeability in the low flow rate regimes for the Bentheimer and Bunter respectively.

The systematic under-prediction in scaling factor is also highlighted by the density function plots in Figure 11b, where the density functions are clearly shifted to the left for the high flow rate calibrations. Despite the shift, the overall bi-modal shape is maintained, with the peaks translating to the high and low capillary pressure regions in both cores. The capillary pressure scaling has therefore been retained in a relative sense, with the difference in entry pressure between the high and low regions the same, but with the overall magnitude altered.

The shift in scaling factors is due to the assumption of capillary pressure equilibrium which is used to initially scale the capillary pressure curves, see Figure 4a. In this work, the initiating assumption effectively means an assumption of $\Delta P_c = 0, N_c = 0$ and that the difference in saturation is solely due to a different capillary pressure curve. However, in the high flow rate experiments N_c is greater than in the low flow rate experiments, with the viscous pressure drop having more of a contributing factor to fluid distribution within the core, reducing the effectiveness of the calibration.

The low capillary number experiment is now simulated with the model using the calibration obtained from observations at high capillary number. The resulting voxel saturation scatter plots comparing the simulated low flow rate

and the experiment are shown in Figure 12. The saturation plots show significant scatter from the identity line. Despite the saturation scatter, the equivalent relative permeability is approximated by the model. The success of the high flow rate calibration is due to the fact that it still captures the relative difference in capillary pressure between the layers, even if the overall magnitude is not fully maintained. With this relative difference, we still predict the lowering of the relative permeability in the perpendicular layering case, and the raising of the gas relative permeability in the parallel layering case. If higher flow rates were chosen, the calibration would become increasingly worse as less information can be derived about capillary heterogeneity.

The total RMS error between simulated and experimental relative permeabilities for the low flow rate experiment is 19.4% and 29.2% for the Bunter and Bentheimer respectively, significantly higher than the capillary limit characterisation result of 9.8% and 18.7% respectively. This highlights the increase in uncertainty incurred as observations underlying the calibration are obtained exclusively at one flow regime.

Care therefore has to be taken when choosing appropriate flow rates for the laboratory experiments when characterising heterogeneity. An ideal situation is to perform two experiments, one at the highest achievable flow rate that still retains a low pore scale capillary number, e.g. $n_c < 10^{-6}$ (governed by allowable pressure drops and fluid re-circulation rates), and the other at the lowest achievable flow rate (governed by measurable pressure drops, pump minimum limits and time). This limits the number of experiments that have to be performed, and permits the greatest amount of characterisation from the available data. Systematic errors are also kept to a minimum by allowing the viscous limit relative permeability to be accurately derived in the high flow rate nearing $\nabla S_w = 0$, along with the capillary pressure calibration nearing $\nabla P_c = 0$.

From these results, it is clear that the capillary pressure heterogeneity can be accurately, and uniquely calibrated using appropriate experimental data, leading to a rock core characterised with intrinsic, rate independent multiphase flow properties. We have extended the work of Krause et al. (2013) and Krause (2012) by incorporating multiple flow rates and fractional flows into the characterisation, using a macroscopic capillary number to guide the conditions at which the multiphase flow properties should be derived. Significant improvements in accuracy are gained by deriving properties in this way, and the predictive capabilities of the resulting numerical model are increased. Attention now turns to using the characterised numerical model in a predictive manner to capture equivalent relative permeabilities outside of those tested in the laboratory.

3.4. Beyond conventional core analysis

Long-standing hurdles in the analysis of heterogeneous rocks come from the impracticalities of purely laboratory based characterisation. The equivalent properties are dependent on flow conditions, fluid properties, and the orientation of heterogeneity with respect to flow. With a numerical model of the rock core, we can now control these conditions to derive the appropriate properties as the basis for further upscaling.

We use the numerical models with relative permeability derived from the observations above the viscous limit and 3D capillary heterogeneity calibrated with observations below the viscous limit. Core flood experiments are simulated across a range of capillary numbers, varied here by altering the flow rate. At each flow rate, we determine the equivalent relative permeability at the core scale by applying Darcy's law using the correct phase pressures in equation (6).

Numerical experiments are presented for three numerical models: 1) The original full length numerical model, with $P_c = 0$ in the end slices. These simulations are representative of a laboratory experiment inclusive of the impact of capillary end effects. 2) The original numerical model with the inlet and outlet 1/7th removed and the outlet slices set to $\tilde{P}_c(S_w)$. This removes the impacts of the boundary conditions, and provides the equivalent property relevant for describing flow in the reservoir system. 3) The same as 2) but with a rotated P_c heterogeneity. As the experimental cores are drilled vertically or horizontally from a reservoir well, there is little control of the orientation of the heterogeneity with respect to the flow direction in the laboratory. By rotating the heterogeneity, we can estimate the relative permeability in a direction perpendicular to the experimental orientation, e.g., an estimate of the horizontal relative permeability can be made using a model calibrated by observations made from a rock core in the vertical orientation.

The capillary pressure heterogeneity is rotated 90° anticlockwise in cubes of 14x14x14 voxels, shown in Figure 13. Only the capillary pressure heterogeneity and porosity are rotated, with all other properties remaining unchanged, meaning the absolute permeability and viscous limit relative permeability also remain unchanged.

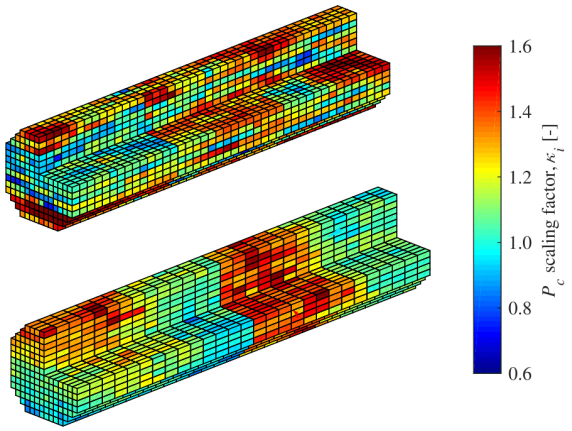

Figure 13: Maps of κ_i in the rotated Bunter (top) and Bentheimer (bottom) cores.

The numerical experiments are conducted across the whole range of the fractional flow curve. We choose specific fractional flows using a distribution between $f_{min} \leq f \leq 1 - f_{min}$, where f_{min} is determined by the minimum flow rate achievable in the numerical simulations. In CMG IMEX the minimum flow rate is ≈ 0.0007 ml.min^{-1}, below the minimum possible in laboratory using 1000D Teledyne ISCO pumps (≈ 0.001 ml.min^{-1}). A geometric distribution of fractional flow points allows population of the fractional curve with many points near the extremes, where a small change in fractional flow causes large changes in core saturation, allowing the full range of experimental saturations to be accessed.

Results at varying N_c using the three numerical models for the Bentheimer and Bunter are shown in Figure 14. Quoted N_c are based on $f_g = 0.5$ fractional flow, since this typically has the largest pressure drop in the experiments due to the competition of both fluids through the pore space and the relatively high effective viscosity of the system.

In Figure 14, the top row of plots using the original, calibrated numerical model clearly highlights the effect of outlet P_c discontinuity (the capillary end effects) when compared to the simulations with the end effect eliminated shown in the second row of plots. The original cores show a large variation of equivalent relative permeability when $N_c < 10$, with both water relative permeabilities significantly reduced relative to the viscous limit values. This is typical of a steady-state relative permeability experiment with significant boundary effects, whereby the discontinuity at the outlet boundary has increased the pressure drop in the water phase, reducing the relative permeability (Krause and Benson, 2015). This effect is significantly reduced for the shortened core with continuous P_c in Figure 14c-d, highlighting the importance of removing the boundary effects in the derivation of the equivalent relative permeability.

In the second row of plots in Figure 14, the equivalent relative permeability curves are shown with the viscous and capillary limit relative permeabilities. The capillary limit relative permeabilities were calculated using the steady-state numerical upscaling technique described in Pickup and Stephen (2000). In summary, we assume capillary equilibrium in the core and scan constant $\tilde{P}_c(S_w)$ values. Given the known 3D capillary pressure heterogeneity in the numerical model, the saturations at every voxel i can be calculated by inverting the individual $P_{c,i}(S_{w,i})$ curves and the corresponding $k_{rj}(S_{w,i})$ found. Single phase, low flow rate core floods are then performed on the numerical model populated with 3D effective absolute permeabilities $k_{rj}(S_{w,i})/k_{abs}$. The resulting steady-state pressure drops at multiple low flow rates can then be used to calculate the effective phase permeability, and through multiplication with the absolute permeability give the equivalent relative permeability for that phase. By selecting $\tilde{P}_c(S_w)$ values across the whole saturation range, the process can be repeated to construct the capillary limit relative permeability curves.

Using the calibrated numerical model in this way, the bounding relative permeability curves can be efficiently derived. In Figure 14c-d the equivalent relative permeability curves converge to the capillary limit at low flow rates and the viscous limit at high flow rates, covering four orders of magnitude in N_c. The deviation from the bounding curves across a large range of flow regimes highlights the importance of equivalent relative permeabilities for modelling subsurface flow, where the flow regime changes significantly between the point of injection and the far field (Reynolds and Krevor, 2015).

The change in equivalent relative permeability from the viscous or capillary limit manifests itself differently for

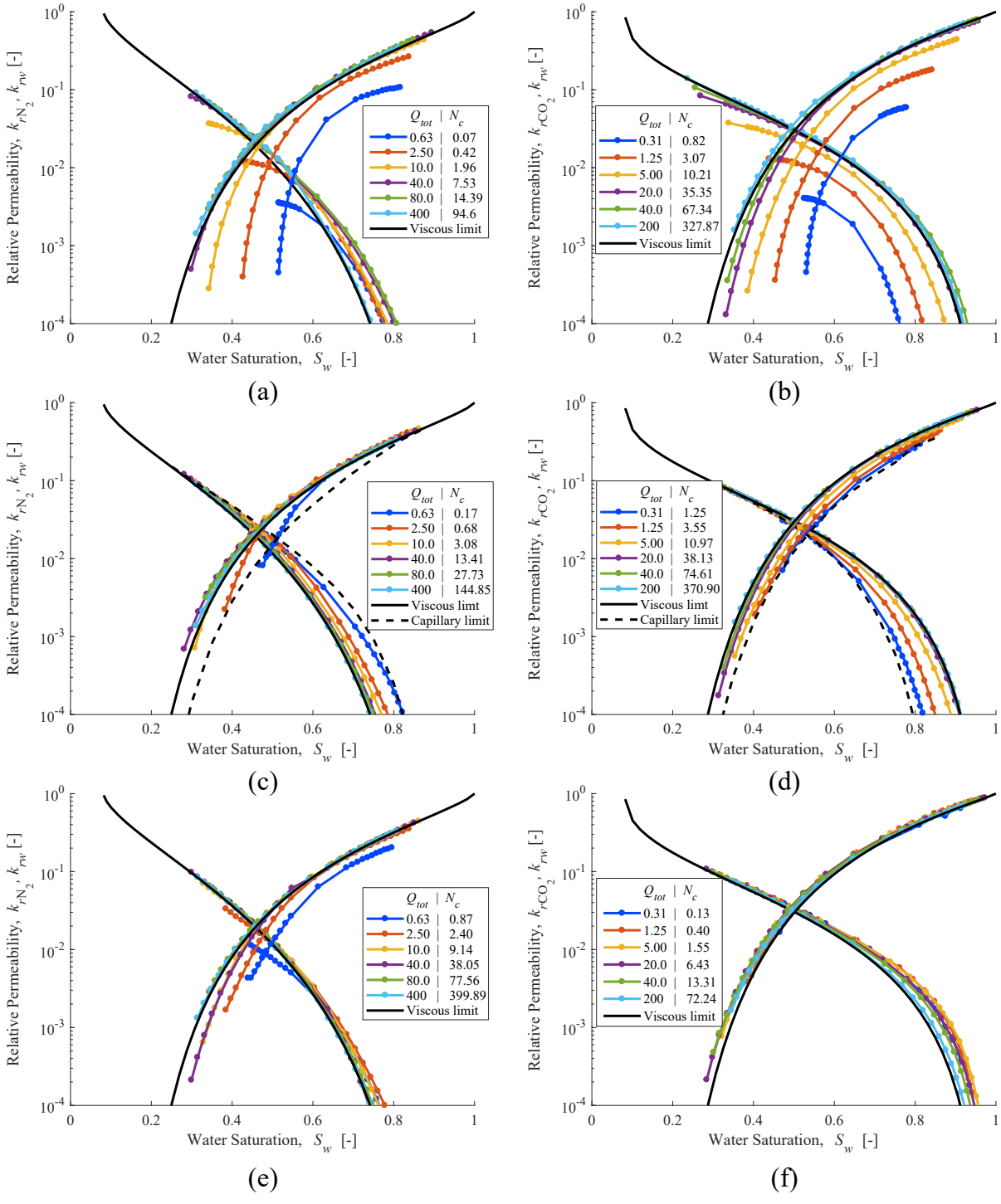

Figure 14: Equivalent relative permeability for the Bentheimer (left) and Bunter (right) sandstone cores at varying flow rates. (a) - (b) Whole core with boundary effects. (c) - (d) Shortened core without boundary effects. (e) - (f) Rotated heterogeneity cores without boundary effects. Q_{tot} has units [ml·min^{-1}] and N_c has units [-].

the Bentheimer and Bunter, depending on the orientation of the capillary pressure heterogeneity. The increase in gas permeability from the viscous limit in the parallel layered Bentheimer in both Figure 14a and c signifies it is a physical effect from the capillary pressure layering, as reported by previous authors (Krause and Benson, 2015; Reynolds and Krevor, 2015; Rabinovich et al., 2016). In the Bunter, we see a different effect, whereby both the gas and water relative permeability curves are lowered below the viscous limit as in Virnovsky et al. (2004); Rabinovich et al. (2016). With combined boundary effects in Figure 14b, the curves have been more significantly reduced, even at high flow rates. This indicates that the impact of capillary heterogeneity in this domain prevails at high capillary number.

In the Bunter sandstone model, by eliminating the boundary discontinuities we significantly change the equivalent relative permeability. This suggests that obtaining equivalent relative permeabilities at low capillary number from laboratory observations alone would be significantly complicated by the presence of the boundary effects of the experiment. With the numerical models, the boundary effects may be eliminated, resulting in the derivation of an equivalent relative permeability representative of flow in the reservoir.

A further experimental constraint that can be removed is the structure of the heterogeneity, which can be re-orientated in the numerical models as seen in Figure 13. The resulting relative permeabilities in Figure 14e-f show show that the characteristic variation with capillary number has now switched for the two rock samples: the re-oriented Bentheimer rock core now has equivalent relative permeabilities that are lower for both phases with decreased capillary number. This is because the layering is now perpendicular to the direction of flow. For the Bunter, the gas phase relative permeability now increases with decreasing capillary number. The re-oriented layering is now perpendicular to the principal direction of flow. The features of the equivalent relative permeability are therefore driven primarily by the orientation of the heterogeneity, as opposed to the rock core itself.

At high fluid saturation in Figures 14c to f, the relative permeability for that particular fluid converge to the same curve regardless of the heterogeneity structure or the capillary number, also seen in Virnovsky et al. (2004) e.g. Figure 6. The relative permeability of the other fluid changes significantly with capillary number at these points, varying by as much as 1.5 orders of magnitude in the results presented here. The functional dependence of the relative permeability on saturation and capillary number can therefore be anchored at the intrinsic values at high gas and water saturations, providing a clear route for potential modelling efforts, and incorporating the relative permeability functional form into simulation packages. We suggest that it is this form of relative permeability that should be used in field scale modelling.

The capillary number at which the saturation distribution and therefore equivalent relative permeability becomes homogeneous is generally reported in the range $10 \leq N_c \leq 100$ (Virnovsky et al., 2004; Reynolds and Krevor, 2015). In Figure 14, the transition to the viscous limit relative permeability does appear to occur when $N_c > 100$ for all systems, even when boundary effects are considered, and represents an upper bound for homogeneity. By removing the boundary effects, we see the transition occur at much lower capillary numbers, around $N_c = 10 - 40$ for the cores in Figure 14c and d, highlighting the care that has to be taken when interpreting the core flood data. The quoted capillary number is that at $f_g = 0.5$, and varies considerably across the range of fractional flows in each experiment, so much so that experiments can transition from the capillary dominated regime to a viscous dominated regime as f_g is varied, see also Reynolds et al. (2017).

To asses the heterogeneity of the system, the scaling factor $\eta = \sigma(P_e)/\mu(P_e)$ can be used, proposed by Li and Benson (2015). For the Bentheimer and Bunter cores in this work, $\eta = 0.155$ and 0.168 respectively, when considering the central sections of each core. This level of hetereogenity is on the lower end of those considered in the work of Li and Benson (2015) where $0.2 < \eta < 0.5$, and similar to the Berea core considered by Pini and Benson (2017), where $\eta \approx 0.1$. Extending this, we use a scaling factor based on an evaluation of saturation heterogeneity to describe the observations. In this way, the impact of the prevailing flow regime is incorporated. The saturation heterogeneity is represented by the scaling factor η_{S_w}:

$$\eta_{Sw} = \sigma(S_w)/\mu(S_w) \tag{11}$$

where $\mu(S_w)$ is the core average saturation and $\sigma(S_w)$ is the standard deviation in saturation through the core. η_{S_w} is presented for the $f_g = 0.5$ fractional flow at different capillary numbers for the numerical experiments in Figure 15. Here, it is clear that after $N_c > 100$, the gradient $\mathrm{d}\eta_{Sw}/\mathrm{d}N_c$ reduces significantly as η_{Sw} approaches zero and the 3D saturation in the core becomes truly homogeneous. Only at this point, when $\eta_{Sw} = 0$ is the core saturation

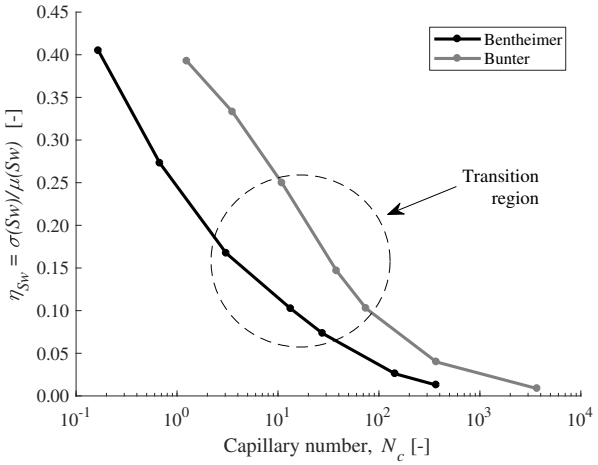

Figure 15: Capillary number N_c against saturation heterogeneity factor η_{Sw} for the shortened Bentheimer and Bunter cores without end effects.

homogeneous, and the viscous limit relative permeability is derived, in practice at $N_c > 40$ when there are no boundary effects. Using N_c, η_{Sw} and η in this way, we can truly judge the level of heterogeneity in the core, and the likely impact on multiphase flow functions.

In the current work, we note that the variation in capillary entry pressures for the bi-model systems is only of the order 300-1500Pa, yet is enough to cause significant capillary number dependency in the relative permeability of the rock samples. Similarly, the heterogeneity factor $\eta \approx 0.16$ is low compared to simulation work by other authors (Li and Benson, 2015; Fourar and Radilla, 2009). We have found significant capillary number dependency in these rocks that would conventionally appear as homogeneous, with capillary number dependence likely to be prominent in almost all but the most homogeneous, isotropic cores, which are not representative of the subsurface. This highlights the shortcomings of conventional core analysis, whereby only the most homogeneous rocks are used to derive the viscous limit relative permeability. A relative permeability derived from such rock samples will have little predictive ability for describing flow in the reservoir system; the concept of the homogeneous rock core therefore has little relevance for a physics based approach to modelling multiphase flow in the subsurface.

The focus of the experimental workflow shifts under this new paradigm; instead of trying to most accurately find a condition invariant relative permeability, we now use the observations under optimised conditions to obtain the most accurate data - viscous limit relative permeability, capillary pressure heterogeneity - for the creation of a numerical rock core. From the numerical model we derive equivalent relative permeabilities that incorporate rock heterogeneity in the relevant orientation and flow rate dependency, to model the effects of mm scale capillary heterogeneity at the cm scale and above. Using the characterised numerical rock core, we can undertake this workflow, producing equivalent relative permeabilities that have a functional dependence on capillary number, saturation and can be direction dependent, as demonstrated in Figure 14. Anisotropic relative permeabilities can occur as a consequence of capillary limit upscaling (Corey and Rathjens, 1956) and can be incorporated into modelling efforts in tensor form akin to the absolute permeability (Keilegavlen et al., 2012).

Given facies distributions in a sub-surface reservoir model, obtained for example through well logs (Babadagli and Al-Salmi, 2004), it is possible to alter the underlying Brooks-Corey model, whilst maintaining the same relative κ_i distribution. With this, 1000s of realisations of different P_e, λ and S_{wirr} zones could be very quickly simulated using sensitivity packages such as CMG CMOST^{TM}, to derive the equivalent relative permeabilities for these systems at varying N_c. Similarly, small-scale geological upscaling as in Pickup and Stephen (2000) and Trevisan et al. (2017a) could make direct use of the experimentally derived κ_i and P_e distributions to link directly with larger numerical upscaling. Using statistical properties of the κ_i distributions, such as variograms and PDFs, these models could generate many realisations of this physically realistic dataset to evaluate sensitivity of the reservoir to slight changes in $P_c(S_w)$ distributions. In this way, the directly measured petrophyiscal properties of the reservoir can inform system sensitivity in a far more realistic way than using purely empirically derived scaling relationships.

4. Conclusions

In this work, we have analysed the characterisation of drainage multiphase flow properties on heterogeneous rock cores, using a combination of experiments and numerical simulation at the mm-m scale. The characterisation was demonstrated using N_2 - DI water and CO_2 - brine systems at reservoir conditions on two sandstones with different principle orientations of heterogeneity, highlighting the applicability of the scheme across a wide range of experimental conditions.

The fundamental experimental observations which informed the characterisation were obtained from steady-state co-injection core floods; the pressure drop through the core at multiple fractional flow rates and the associated 3D saturation maps inside the core obtained at mm scale through medical X-ray imaging. Only two experiments had to be performed for each core; an experiment at high flow rate, which allowed characterisation of the viscous limit relative permeability and absolute permeability, and an experiment at low flow rate below the viscous limit, which allowed evaluation of the capillary pressure heterogeneity. Through scaling of the average capillary pressure curve in the rock core with a simple scaling factor κ_i, the capillary pressure heterogeneity at the mm scale was evaluated in 3D using the experimentally observed saturation at low flow rate.

Upon calibration of the numerical model against observed millimetre scale saturation heterogeneity, we accurately predict average pressure drop at the core scale and equivalent relative permeabilities. We also showed how a numerical model calibrated using a single, high flow rate dataset could predict low flow rate experimental equivalent permeabilities with minor loss in accuracy, as long as some level of saturation heterogeneity prevailed in the high flow rate regime.

The calibrated numerical models were used to estimate equivalent relative permeabilities across capillary numbers ranging from $0.07 \leq N_c \leq 400$, roughly four orders of magnitude. We showed that the main features of equivalent relative permeabilities for parallel and perpendicular layered heterogeneous systems in the upscaled capillary limit were predicted as $N_c \rightarrow 0$. As the fluid saturation approached unity, we also found that the relative permeabilities converged to the same curve, regardless of the capillary number. This observation provides a possible route for future modelling efforts, where a capillary number, saturation and direction dependent equivalent relative permeability function could be anchored to the same curve as $S_j \rightarrow 1$.

Removal of boundary effects inherent with experimental core floods, and re-structuring of the heterogeneity in the final results section highlighted the applicability of the approach for advanced core characterisation. The derived numerical model could be used without the limitations imposed by the experiment to derive meaningful equivalent relative permeabilities representative of the flow in the subsurface. These flow functions can then be used directly in modelling efforts to more accurately simulate plume evolution and capillary trapping associated with low potential flows in the subsurface.

The characterisation presented in this paper represents a first step in obtaining a completely parameterised numerical model for use in reservoir characterisation. Future work aims to analyse the drainage process on other rock cores with multi-level heterogeneity, e.g. carbonate rocks, and to extend the approach to incorporate flow hysteresis and trapping.

Acknowledgments

This work was funded by the Natural Environment Research Council (Grant number: NE/N016173/1). We acknowledge PRORES and Computer Modelling Group for providing access to SENDRA and IMEX respectively. Data associated with this work may be obtained by contacting samuel.jackson@imperial.ac.uk.

References

Akbarabadi, M., Piri, M., 2012. Relative permeability hysteresis and capillary trapping characteristics of supercritical CO_2/brine systems: an experimental study at reservoir conditions. Advances in Water Resources 52, 190–206.

Akin, S., Kovscek, A., 2003. Computed tomography in petroleum engineering research. Vol. 215. pp. 23–38.

Armstrong, R., Georgiadis, A., Ott, H., Klemin, D., Berg, S., 2014. Critical capillary number: Desaturation studied with fast X-ray computed microtomography. Geophysical Research Letters 41, 55–60.

Babadagli, T. ., Al-Salmi, S., 2004. A review of permeability-prediction methods for carbonate reservoirs using well-log data. SPE Reservoir Evaluation & Engineering, 75–88.

Bachu, S., Bennion, B., 2008. Effects of in-situ conditions on relative permeability characteristics of CO_2-brine systems. Environmental Geology 54, 1707–1722.
Barker, J., Dupouy, P., 1999. An analysis of dynamic pseudo-relative permeability methods for oil-water flows. Petroleum Geoscience 5, 385–394.
Cavanagh, A., Nazarian, B., 2014. A new and extended Sleipner benchmark model for CO_2 storage simulations in the Utsira formation. Energy Procedia 63, 2831–2835.
Chierici, G., 1984. Novel relations for drainage and imbibition relative permeabilities. SPE Journal, 275–276.
Corbett, P., Ringrose, P., Jensen, J., Sorbie, K., 1992. Laminated clastic reservoirs: The interplay of capillary pressure and sedimentary architecture. In: 67th Annual Technical Conference and Exhibition of the Society of Petroleum Engineers, Washington D.C., October 4-7, 1992. No. SPE 24699.
Corey, A. T., Rathjens, C. H., 12 1956. Effect of stratification on relative permeability. Journal of Petroleum Technology 8, 69–71.
Dagan, G., Fiori, A., Jankovic, I., 2013. Upscaling of flow in heterogeneous porous formations: Critical examination and issues of principle. Advances in Water Resources 51, 67–85.
Dumore, J., Schols, R., 1974. Drainage capillary-pressure functions and the influence of connate water. Society of Petroleum Engineers Journal 14 (5), 437–444.
Durlofsky, L., 1991. Numerical calculation of equivalent grid block permeability tensors for heterogeneous porous media. Water Resources Research 27 (5), 699–708.
Egermann, P., Lenormand, R., 2005. A new methodology to evaluate the impact of localized heterogeneity on petrophysical parameters (k_r, p_c) applied to carbonate rocks. Petrophysics 46 (5), 335–345.
Fernandes, J., Appoloni, C., Fernandes, C., 2012. Determination of the representative elementary volume for the study of sandstones and siltstones by X-Ray microtomography. Materials Research 15 (4), 662–670.
Fourar, M., Radilla, G., 2009. Non-fickian description of tracer transport through heterogeneous porous media. Transport in Porous Media 80, 561–579.
Fulcher Jr., R., Ertekin, T., Stahl, C., 1985. Effect of capillary number and its constituents on two-phase relative permeability curves. Journal of Petroleum Technology 37 (2), 249–260.
Gasda, S., Celia, M., 2005. Upscaling relative permeabilities in a structured porous medium. Advances in Water Resources 28, 493–506.
Holden, L., Nielsen, B. F., 2000. Global upscaling of permeability in heterogeneous reservoirs; The output least squares (OLS) method. Transport in Porous Media 40 (2), 115–143.
Honarpour, M., Cullick, A., Saad, N., Humphreys, N., 1995. Effect of rock heterogeneity on relative permeability: Implications for scaleup. Journal of Petroleum Technology 47 (11), 980–986.
Honarpour, M., Koederitz, F., Herbert, A., 1986. Relative permeability of petroleum reservoirs. CRC Press Inc, Boca Raton, FL.
Hovorka, S. D., Benson, S. M., Doughty, C., Freifeld, B. M., Sakurai, S., Daley, T. M., Kharaka, Y. K., Holtz, M. H., Trautz, R. C., Nance, H. S., Myer, L. R., Knauss, K. G., 2006. Measuring permanence of CO_2 storage in saline formations: the frio experiment. Environmental Geosciences 13 (2), 105–121.
Huang, Y., Ringrose, P., Sorbie, K., 1995. Capillary trapping mechanisms in water-wet laminated rocks. SPE Reservoir Engineering 10, 287–292.
Jackson, M. D., Muggeridge, A. H., Yoshida, S., Johnson, H. D., 2003. Upscaling permeability measurements within complex heterolithic tidal sandstones. Mathematical Geology 35, 499–520.
Keilegavlen, E., Nordbotten, J. M., Stephansen, A. F., 2012. Tensor relative permeabilities: Origins, modeling and numerical discretization. International Journal of Numerical Analysis and Modeling 9 (3), 701–724.
Krause, M., 2012. Modeling and investigation of capillary heterogeneity on multiphase flow of CO_2 and brine. Ph.D. thesis, Stanford University.
Krause, M., Benson, S., 2015. Accurate determination of characteristic relative permeability curves. Advances in Water Resources 83, 376–388.
Krause, M., Krevor, S., Benson, S., 2013. A procedure for the accurate determination of sub-core scale permeability distributions with error quantification. Transport in Porous Media 93 (3), 565–588.
Krevor, S., Pini, R., Li, B., Benson, S., 2011. Capillary heterogeneity trapping of CO_2 in a sandstone rock at reservoir conditions. Geophysical Research Letters 38, L15401.
Krevor, S., Pini, R., Zuo, L., Benson, S., 2012. Relative permeability and trapping of CO_2 and water in sandstone rocks at reservoir conditions. Water Resources Research 48 (2), W02532.
Kuo, C.-W., Benson, S., 2013. Analytical study of effects of flow rate, capillarity, and gravity on CO_2/brine multiphase-flow system in horizontal corefloods. SPE Journal 18 (4), 708–720.
Li, B., Benson, S., 2015. Influence of small-scale heterogeneity on upward CO_2 plume migration in storage aquifers. Advances in Water Resources 83, 389–404.
McPhee, C., Reed, J., Zubizarreta, I., 2015. Core Analysis: A best practice guide. Vol. 64.
Meckel, T., Bryant, S., Ganesh, P. R., 2015. Characterization and prediction of CO_2 saturation resulting from modeling buoyant fluid migration in 2D heterogeneous geologic fabrics. International Journal of Greenhouse Gas Control 34, 85–96.
Nordahl, K., Ringrose, P. S., Wen, R., 2005. Petrophysical characterization of a heterolithic tidal reservoir interval using a process-based modelling tool. Petroleum Geoscience 11, 17–28.
Oak, M., 1980. Three-phase relative permeability of water-wet berea. In: SPE/DOE Seventh Symposium on Enhanced Oil Recovery, Tulsa, Oklahoma.
Odsæter, L., Berg, C., Rustad, A., 2015. Rate dependency in steady-state upscaling. Transport in Porous Media 110, 565–589.
Peksa, A., Wolf, K.-A., Zitha, P., 2015. Bentheimer sandstone revisited for experimental purposes. Marine and Petroleum Geology 67, 701–719.
Pentland, C., El-Maghraby, R., Iglauer, S., Blunt, M., 2011. Measurements of the capillary trapping of super-critical carbon dioxide in berea sandstone. Geophysical Research Letters 38 (6), L06401.
Perrin, J.-C., Benson, S., 2010. An experimental study on the influence of sub-core scale heterogeneities on CO_2 distribution in reservoir rocks. Transport in Porous Media 82 (1), 93–109.
Pickup, G. E., Stephen, K. D., 2000. An assessment of steady-state scale-up for small-scale geological models. Petroleum Geoscience 6, 203–210.
Pini, R., Benson, S., 2013a. Characterization and scaling of mesoscale heterogeneities in sandstones. Geophysical Research Letters 40, 3903–3908.

Pini, R., Benson, S., 2013b. Simultaneous determination of capillary pressure and relative permeability curves from core-flooding experiments with various fluid pairs. Water Resources Research 49, 3516–3530.
Pini, R., Benson, S., 2017. Capillary pressure heterogeneity and hysteresis for the supercritical CO_2/water system in a sandstone. Advances in Water Resources 108, 277–292.
Pini, R., Krevor, S., Benson, S., 2012. Capillary pressure and heterogeneity for the CO_2/water system in sandstone rocks at reservoir conditions. Advances in Water Resources 38, 48–59.
Pini, R., Madonna, C., 2016. Moving across scales: a quantitative assessment of X-ray CT to measure the porosity of rocks. Journal of Porous Material 23, 325–338.
Rabinovich, A., Itthisawatpan, K., Durlofsky, L., 2015. Upscaling of CO_2 injection into brine with capillary heterogeneity effects. Journal of Petroleum Science and Engineering 134, 60–75.
Rabinovich, A., Li, B., Durlofsky, L., 2016. Analytical approximations for effective relative permeability in the capillary limit. Water Resources Research 52 (4), 7645–7667.
Renard, P., de Marsily, G., 1997. Calculating equivalent permeability: a review. Advances in Water Resources 20 (5-6), 253–278.
Reynolds, C., Blunt, M., Krevor, S., 2017. Multiphase flow characteristics and heterogeneity of rocks from CO_2 storage reservoirs in the United Kingdom. Under review.
Reynolds, C., Krevor, S., 2015. Characterizing flow behaviour for gas injection: Relative permeability of CO_2-brine and N_2-water in heterogeneous rocks. Water Resources Research 51 (12), 9464–9489.
Ringrose, P., Bentley, M., 2015. Reservoir Model Design. A Practitioners Guide. Springer, Dordrecht.
Ringrose, P., Corbett, P., 1994. Controls on two-phase fluid flow in heterogeneous sandstones. Geological Society, London, Special Publications 78, 141–150.
Ringrose, P., Sorbie, K., Corbett, P., Jensen, J., 1993. Immiscible flow behaviour in laminated and cross-bedded sandstones. Journal of Petroleum Science and Engineering 9, 103–124.
Saad, N., Cullick, A., Honarpour, M., 1995. Effective relative permeability in scale-up and simulation. In: SPE Rocky Mountain Regional/Lew-Permeability Symposium, Denver, Colorado, March 20-22, 1995. No. SPE 29592.
Saadatpoor, E., Bryant, S. L., Sepehrnoori, K., 2010. New trapping mechanism in carbon sequestration. Transport in Porous Media 82, 3–17.
Shi, J.-Q., Xue, Z., Durucan, S., 2011. Supercritical CO_2 core flooding and imbibition in tako sandstone - influence of sub-core scale heterogeneity. International Journal of Greenhouse Gas Control 5 (1), 75–87.
Trevisan, L., Krishnamurthyb, P., MeckelaaGulf, T., 2017a. Impact of 3D capillary heterogeneity and bedform architecture at the sub-meter scale on CO_2 saturation for buoyant flow in clastic aquifers. International Journal of Greenhouse Gas Control 56, 237–249.
Trevisan, L., Pini, R., nd J.T. Birkholzer, A. C., Zhou, Q., González-Nicolás, A., Illangasekare, T., 2017b. Imaging and quantification of spreading and trapping of carbon dioxide in saline aquifers using meter-scale laboratory experiments. Water Resources Research 53 (1), 485–502.
Virnovsky, G., Friis, H., Lohne, A., 2004. A steady-state upscaling approach for immiscible two-phase flow. Transport in Porous Media 54, 167–192.
Wei, N., Gill, M., Crandall, D., McIntyre, D., Wang, Y., Bruner, K., Li, X., Bromhal, G., 2014. CO_2 flooding properties of liujiagou sandstone: influence of sub-core scale structure heterogeneity. Greenhouse Gases: Science and Technology 4 (3), 400–418.
Zhang, D., Zhang, R., Chen, S., Soll, W., 2000. Pore scale study of flow in porous media: Scale dependency, REV, and statistical REV. Geophysical Research Letters 27 (8), 1195–1198.